Progress in Oceanography 172 (2019) 14–33

Contents lists available at ScienceDirect

Progress in Oceanography

journal homepage: www.elsevier.com/locate/pocean

Circulation of the Chukchi Sea shelfbreak and slope from moored timeseries

Min Li[a,b,c,d,*], Robert S. Pickart[b], Michael A. Spall[b], Thomas J. Weingartner[e], Peigen Lin[b], G.W.K. Moore[f], Yiquan Qi[g]

[a] State Key Laboratory of Tropical Oceanography, South China Sea Institute of Oceanology, Chinese Academy of Sciences, Guangzhou, Guangdong 510301, China
[b] Woods Hole Oceanographic Institution, Woods Hole, MA 02543, USA
[c] Guangdong Province Key Laboratory for Coastal Ocean Variation and Disaster Prediction, Guangdong Ocean University, Zhanjiang, Guangdong 524088, China
[d] University of Chinese Academy of Sciences, Beijing 100049, China
[e] Institute of Marine Science, University of Alaska, Fairbanks, AK 99775, USA
[f] Department of Physics, University of Toronto, Toronto, Ontario, Canada
[g] College of Oceanography, Hohai University, Nanjing, Jiangsu 210098, China

ARTICLE INFO

Keywords:
Circulation
Chukchi Sea
Boundary currents
Arctic
Shelfbreak upwelling

ABSTRACT

Data from a year-long mooring array across the shelfbreak/upper-slope of the Chukchi Sea are used to describe and quantify the circulation and water masses of the region. The timeseries revealed the year-round existence of the eastward-flowing shelfbreak jet and, seaward of this, the westward-flowing Chukchi Slope Current. In the mean the slope current is estimated to transport 0.57 ± 0.04 Sv of Pacific water, while the bottom-intensified shelfbreak jet transports 0.009 ± 0.003 Sv towards Barrow Canyon. The slope current is surface-intensified in summer and fall, and in winter and spring it becomes middepth-intensified, moves shoreward, and weakens. Two extreme states of the circulation were identified: (1) an enhanced slope current and reversed (westward-flowing) shelfbreak jet; and (2) a strong eastward-flowing shelfbreak jet and weak slope current. The former state occurs when the wind stress curl on the Chukchi shelf is positive, and the latter state occurs when the curl is negative. A simple theoretical model is used to determine the changes in sea surface height due to such wind stress curl forcing, which is consistent with the observed changes in flow seaward of the shelf – both in amplitude and phase – via geostrophic set up. Shelfbreak upwelling occurred throughout the year, but there was no correlation between the regional wind conditions and the upwelling. Furthermore, there was no apparent relationship between upwelling and the extreme slope current/shelfbreak jet events. A comparison of water mass signals between the Chukchi slope array and a mooring at the head of Barrow Canyon supports the notion that the slope current is fed by the outflow of Pacific water from the canyon.

1. Introduction

The Pacific inflow through Bering Strait, driven by the large-scale sea level gradient between the Pacific and Arctic Oceans (Stigebrandt, 1984), plays a key role in the regional ecosystem of the Chukchi Sea and Canada Basin (Aagaard and Carmack, 1989; Walsh, 1995; Mathis et al., 2007; Pickart et al., 2016). The Pacific-origin water carries nutrients, heat, and freshwater into the Chukchi Sea which, among other things, impacts the circulation and stratification of the shelf, the growth of phytoplankton, and the distribution of sea ice (Weingartner et al., 2005; Hill and Cota, 2005; Yang, 2006; Shimada et al., 2006; Woodgate et al., 2010; Spall et al., 2014). After some degree of modification on the Chukchi shelf, the water is then fluxed into the Canada Basin via different mechanisms of shelf-basin exchange, where it has a profound effect on the chemical and physical properties of the interior halocline (Jones and Anderson, 1986; Steele et al., 2004; Pickart et al., 2005; Spall et al., 2008; Toole et al., 2010).

It is generally believed that there are three main, topographically steered pathways by which Pacific water flows poleward through the Chukchi Sea (Weingartner et al., 2005; see Fig. 1). The western pathway progresses through Herald Canyon between Wrangel Island and Herald Shoal; the central pathway flows through the Central Channel between Herald and Hanna Shoals; and the eastern pathway flows adjacent to the Alaskan coast from Cape Lisburne to Barrow Canyon. In summertime this branch is known as the Alaskan coastal current (ACC; Paquette and Bourke, 1974). Recent work has suggested that the central branch forms a number of smaller filaments as it flows towards Hanna Shoal (Pickart et al., 2016; Fig. 1). The precise

* Corresponding author at: College of Ocean and Meteorology, Guangdong Ocean University, Zhanjiang, Guangdong 524088, China.
E-mail address: limin_gdou@hotmail.com (M. Li).

https://doi.org/10.1016/j.pocean.2019.01.002
Received 2 June 2018; Received in revised form 12 December 2018; Accepted 4 January 2019
Available online 09 January 2019
0079-6611/

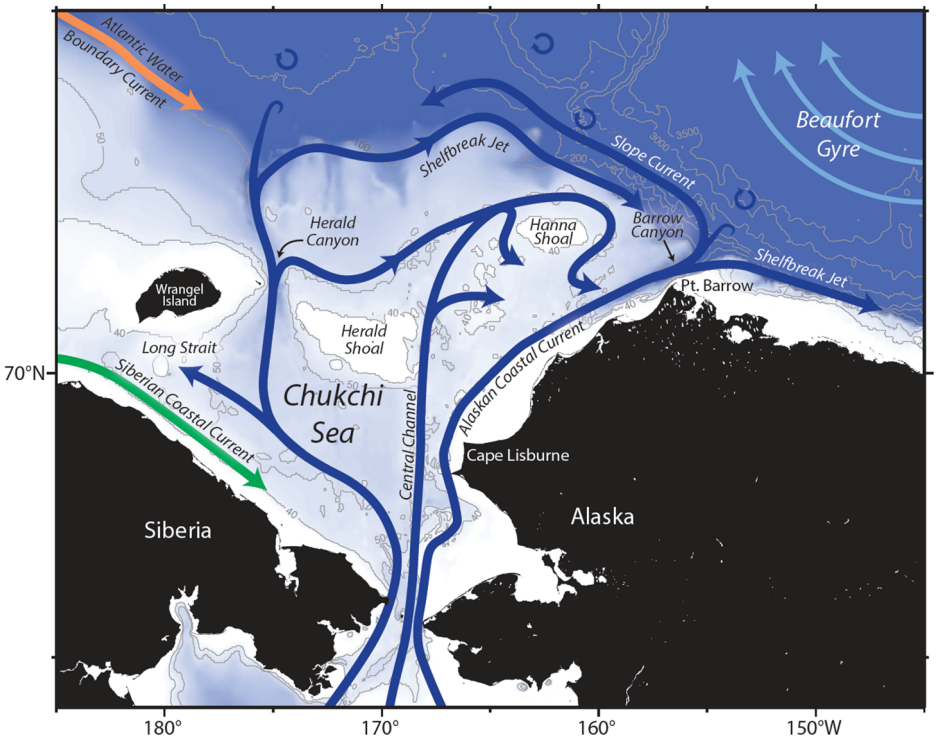

Fig. 1. Schematic circulation in the Chukchi Sea (from Corlett and Pickart, 2017), showing the three main pathways by which Pacific water flows poleward through the Chukchi Sea.

partitioning of transport between the three branches remains uncertain. Woodgate et al. (2005) suggest that, averaged over the year, the division of transport is roughly equal. However, their study was based on a limited number of moorings. On the other hand, various studies have suggested that, at least during the summer months, much of the Pacific water flowing through Bering Strait is eventually channeled into Barrow Canyon via the central and eastern pathways. (Itoh et al., 2013; Gong and Pickart, 2015; Pickart et al., 2016; Weingartner et al., 2017).

There is also uncertainty as to how and where the Pacific water exits the Chukchi shelf into the Canada Basin. A portion of the outflow from Barrow Canyon turns eastward along the edge of Beaufort Sea to form the Beaufort shelfbreak jet (Pickart, 2004; Nikolopoulos et al., 2009). Using data from a high-resolution mooring array, the year-long mean transport of the jet from summer 2002 to summer 2003 was estimated to be 0.13 ± 0.08 Sv (Nikolopoulos et al., 2009). However, Brugler et al. (2014) demonstrated that this transport dropped by more than 80% later in the decade, suggesting that the Beaufort shelfbreak jet can only account for a small fraction of the Bering Strait inflow. Some of the Pacific water also exits the Chukchi shelf through Herald Canyon and forms an eastward-flowing shelfbreak jet along the edge of the Chukchi Sea (Mathis et al., 2007; Pickart et al., 2010; Linders et al., 2017; Corlett and Pickart, 2017). A portion of the water also appears to enter the East Siberian Sea through Long Strait (Woodgate et al., 2005), although this has not yet been established as a permanent pathway. Recently, Timmermans et al. (2017) argued that some of the Pacific water is fluxed into the Canada Basin via subduction along the entire edge of the Chukchi shelf.

The long-term mean northward transport of Pacific water at the mouth of Barrow Canyon has been estimated to be 0.44 Sv (Itoh et al., 2013), which is far greater than the eastward transport of the Beaufort shelfbreak jet. The obvious question then is, where does the bulk of the Pacific water go upon exiting the canyon? Recent work has documented the existence of a westward-flowing current along the continental slope of the Chukchi Sea. Using hydrographic and velocity data from 46 shipboard transects across the shelfbreak/slope of the Chukchi Sea between 2002 and 2014, Corlett and Pickart (2017) revealed the presence of the current which is surface-intensified and order 50 km wide during the summer months (July-October). The strongest flow occurs within 25 km of the shelfbreak. Corlett and Pickart (2017) named the current the Chukchi Slope Current, and estimated the transport of Pacific water to be 0.50 ± 0.07 Sv. It was argued that the current is formed from the outflow from Barrow Canyon, and, using their data together with historical measurements, Corlett and Pickart (2017) constructed a mass budget of the Chukchi shelf where the inflows and outflows balance each other within the estimated errors. Recently published drifter data support the notion that the outflow from Barrow Canyon forms the slope current (Stabeno et al., 2018).

Two recent modeling studies have also addressed aspects of the Chukchi Slope Current. Watanabe et al. (2017) investigated the advection of Pacific water during the winter months from Barrow Canyon to the Chukchi Plateau. Their model revealed a persistent westward-flowing current that they referred to as a “shelfbreak flow”, but it is clear that this is the slope current. A tracer analysis indicated that the source was Barrow Canyon. The wintertime model current was mid-depth intensified, in contrast to the summertime surface-intensified current identified by the observations of Corlett and Pickart (2017). The second modeling study investigated the means by which Pacific-origin water enters the Canada Basin (Spall et al., 2018). The model indicated that most of the Pacific water feeding the basin (i.e. crossing the isobaths of the outer shelf) did so in Barrow Canyon. This downplays the importance of the shelf-basin subduction mechanism proposed by Timmermanns et al. (2017). Furthermore, in Spall et al.’s (2018) model much of the Pacific water emanating from Barrow Canyon turned westward and formed a current over the continental slope, in line with the observations. Notably, the slope current was distinct from the Beaufort Gyre.

In addition to the westward-flowing Chukchi Slope Current, Corlett and Pickart (2017) also quantified the presence of the eastward-flowing Chukchi Shelfbreak Jet (Fig. 1), whose existence was implied previously from mainly anecdotal evidence. Using the large number of shipboard transects, Corlett and Pickart (2017) estimated the jet’s mean summertime transport to be 0.10 ± 0.03 Sv. Although the mean flow is eastward, at times it can flow to the west. Corlett and Pickart (2017)

argued that this reversed flow happens during times of easterly winds. It is thought that the jet gets entrained into the Chukchi Slope Current at the mouth of Barrow Canyon (Fig. 1).

One of the dominant mechanisms of shelf-basin exchange across the edge of the Beaufort Sea is wind-driven upwelling (Pickart et al., 2009; Pickart et al., 2011; Lin et al., 2018). Easterly winds, arising from the intensification of the Beaufort High and/or passing Aleutian Lows to the south, readily reverse the Beaufort shelfbreak jet and drive water from the slope onto the shelf. This occurs during all seasons of the year and under different ice conditions (Schulze and Pickart, 2012). Evidence of upwelling on the Chukchi slope is far less conclusive. Llinás et al. (2009) suggested the occurrence of upwelling based on a single shipboard transect north of Hanna Shoal, characterized by the presence of Atlantic water on the upper slope as well as surface-intensified westward flow which they interpreted as a reversed shelfbreak jet. Using observations and a simplified numerical model, Spall et al. (2014) argued that upwelling of nutrients from the halocline to the outer shelf north of Central Channel contributed to the massive under-ice phytoplankton bloom reported by Arrigo et al. (2014). Recently, Corlett and Pickart (2017) presented evidence that the westward-flowing Chukchi Slope Current is intensified under enhanced easterly winds. However, more extensive measurements are necessary to robustly establish the occurrence of upwelling along the Chukchi slope and its forcing mechanisms.

This study presents results from a mooring array that was deployed across the shelfbreak and slope of the Chukchi Sea from October 2013 to September 2014 to the northeast of Hanna Shoal. It is the first set of high spatial resolution timeseries obtained from the region. The primary aim of the study is to elucidate the structure and transport of both the Chukchi Shelfbreak Jet and the Chukchi Slope Current, and to identify the nature and causes of the variability of the two currents. We begin with a presentation of the different sources of data used in the study in Section 2, followed in Section 3 by an investigation of the mean structure and seasonality of the circulation and hydrography. In Section 4 the volume transport of the shelfbreak jet and slope current, as well as their correlation, are addressed. In Section 5 we consider the strong/weak states of the two currents using a composite analysis. The occurrence of upwelling is then investigated in Section 6, followed by consideration of the propagation of water mass signals from Barrow Canyon into the slope current in Section 7.

2. Data and methods

The data used in this study were collected as part of a year-long field program funded by the Bureau of Ocean and Energy Management (BOEM) entitled “Characterization of the Circulation on the Continental Shelf Areas of the Northeast Chukchi and Western Beaufort Seas”. The program employed moorings, gliders, drifters, and included multiple shipboard surveys. The present analysis uses primarily the mooring data, along with various ancillary data sets.

2.1. Mooring data

From October 2013 to September 2014, six moorings (CS1-5 and FM1) were deployed across the shelfbreak and slope of the Chukchi Sea (Fig. 2, CS1 is not shown because it is not used in present study). All of the moorings were equipped with an upward-facing acoustic Doppler current profiler (ADCP, 300KHz or 75KHz) near the bottom, which provided hourly velocity profiles with a vertical resolution of 5–10 m. Hydrographic properties were measured by MicroCATs situated next to the ADCPs, and with two types of conductivity-temperature-depth (CTD) profilers: a Coastal Winched Profiler (CWP) at FM1, and Coastal Moored Profilers (CMPs) at every site. The CMPs provided vertical traces of temperature and salinity nominally four times per day with a vertical resolution of 2 m, while the CWP produced profiles once per day with a resolution of 1 m. A detailed summary of the mooring components is contained in Table 1.

All of the ADCPs and MicroCATs returned year-long records. Unfortunately, the moored profiler coverage was generally poor. The CWP at FM1 failed immediately after being deployed.[1] Of the CMPs, only the one at CS4 profiled for the entire duration of the deployment. The instrument at CS5 profiled for eight months, the one at CS3 for two months, and the one at FM1 not at all. In the latter two instances, however, the CTD sensor on the profiler remained operational at a fixed depth, acting as a de facto MicroCAT. The CMP at CS2 failed entirely. Details regarding the mooring instrumentation and data coverage are found in Table 1.

Three additional moorings (NE40, NE50, NE60) were maintained from September 2013 to September 2014 on the eastern side of Hanna Shoal at roughly the 40 m, 50 m, and 60 m isobaths (Fig. 2b). Together, the two sets of moorings comprise an array extending from the edge of Hanna Shoal across the shelfbreak to the upper slope. The shelf moorings were equipped with ADCPs and MicroCATs at the bottom, recording velocity twice per hour and hydrographic data four times per hour. The vertical resolution of the ADCPs was 1 m. Velocity profiles with the same vertical resolution and daily-averaged hydrographic data from a mooring at the head of Barrow Canyon (BC2, Fig. 2b) were also used for part of the analysis. The reader should consult Weingartner et al. (2017) for details about the configuration of this mooring.

All of the velocity data were de-tided using the T_Tide harmonic analysis toolbox (Pawlowicz et al., 2002). This revealed that there was low tidal energy level across the array: the maximum amplitude of the eight dominant tidal constituents was found to be less than 2.2 cm/s, which is considerably smaller than the sub-tidal signals of interest. The inertial signal was also found to be generally insignificant. A rotated coordinate system was used in the analysis. The along-stream direction was determined by averaging the year-long mean, depth-integrated velocity vectors at the five outer moorings. The positive x (along-stream) direction is defined as southeastward (138°T) and the positive y (cross-stream) direction is northeastward (48°T, Fig. 2b). The associated velocities are referred to as u and v, respectively. Vertical sections of the two components of velocity were constructed at each time step using Laplacian-spline interpolation, with a horizontal grid spacing of 2 km and vertical grid spacing of 15 m. The domain of the vertical sections is limited to the five outer moorings, i.e. the region of the shelfbreak and slope, which is the main focus of the study.

2.2. Wind data

Wind timeseries from the Barrow, AK meteorological station are used in the study. The site is roughly 120 km to the southeast of the array. The data were obtained from the National Climate Data Center (NODC) of the National Oceanic and Atmospheric Administration (NOAA) and have been quality controlled and interpolated to an hourly time base. The reader is referred to Pickart et al. (2013) for details.

2.3. Atmospheric reanalysis fields

To assess the effect of the broad-scale atmospheric forcing, we used reanalysis data from the North American Regional Reanalysis (NARR, Mesinger et al., 2006). This includes sea level pressure and 10 m wind fields with a lateral resolution of 32 km and time resolution of 6 h. The NARR product represents an improvement on the global National Centers for Environmental Prediction (NCEP) reanalysis dataset in this region in resolution. The correlation between the Barrow wind timeseries and the NARR wind record in the vicinity of moorings is 0.8, at a confidence level of 95%.

2.4. Ice concentration and velocity data

The ice concentration data used in the study are the Advanced Very High Resolution Radiometer (AVHRR) product from NODC, NOAA. The

[1] The CWP at mooring CS1 lasted for approximately one month, but those data are not considered in this study.

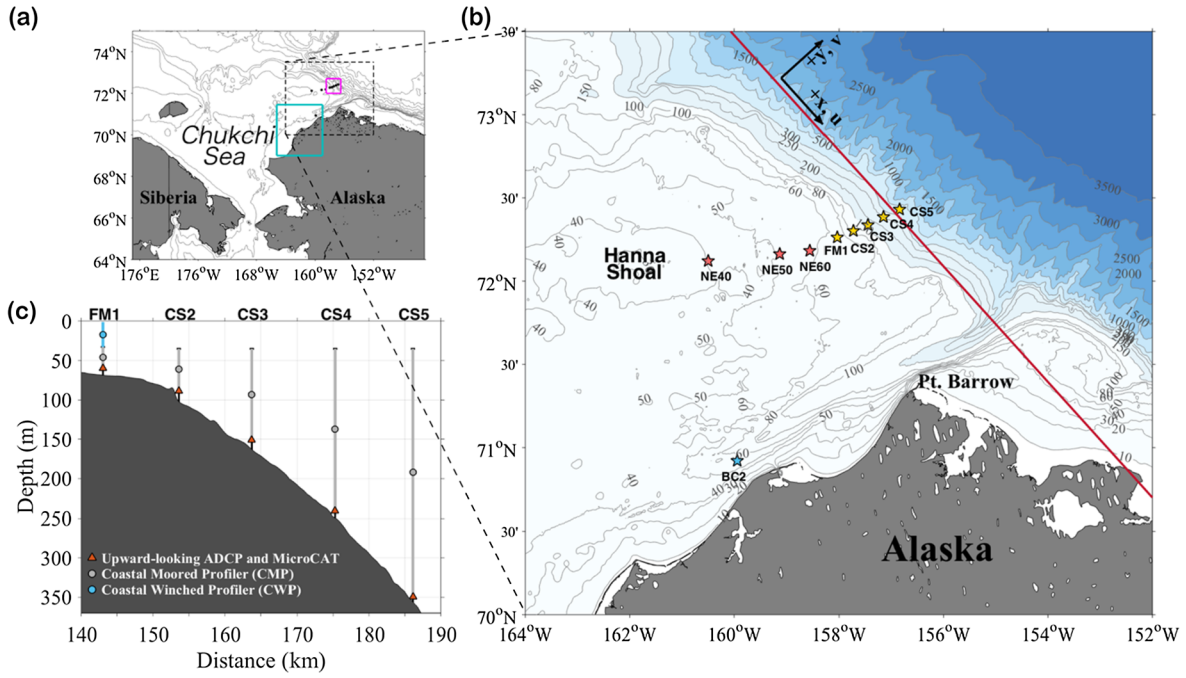

Fig. 2. (a) Large-scale map showing the Chukchi Sea. The region in (b) is indicated by the dashed box. The magenta and cyan boxes delineate the domain over which the ice concentration is calculated for the shelfbreak/slope array and for the coastal polynya region south of Barrow Canyon, respectively. The mooring sites are indicated by the black dots. (b) Zoomed-in map of the northeastern Chukchi Sea showing the locations of the moorings used in the study. The five moorings comprising the shelfbreak/slope array are shown by the yellow stars. The three additional moorings east of Hanna Shoal and the mooring at the head of Barrow Canyon are shown by the red and blue stars, respectively. The red line and black coordinate frame indicate the rotated coordinate system. The bathymetry is from IBCAO v3. (c) Configuration of shelfbreak/slope moorings in the vertical plane. The origin of the distance axis is Hanna Shoal. (For interpretation of the references to colour in this figure legend, the reader is referred to the web version of this article.)

spatial and temporal resolution of the data are 0.25° and once per day. We constructed a timeseries of ice concentration for the location of the array by averaging the data within the magenta box in Fig. 2a. To assess the polynya activity south of Barrow Canyon we averaged the data within the cyan box in Fig. 2a. The sea ice velocity data are from version 3 of the Polar Pathfinder daily sea ice motion dataset (Tschudi et al., 2016). The dataset uses a blend of inputs from a variety of sources (IABP buoy motion, NCEP/NCAR Winds, SSM/I, SSMIS, SMMR, AMSR-E, and AVHRR) to estimate daily ice motion. The horizontal resolution of the product is 25 km.

2.5. Regional numerical model

An analytic theory and regional numerical model are used to provide a dynamical framework for the interpretation of the influence of winds on the circulation on the outer shelf and slope. The model is the MITgcm (Marshall et al., 1997) configured in a domain that spans the Chukchi Sea and southern Canada Basin. Similar models were used by Spall (2007) and Pickart et al. (2011). The model topography was interpolated from the ETOPOv2 global topography on a 2-minute grid to the model grid with 10 km horizontal grid spacing and 30 levels in the vertical (5 m vertical grid spacing over the Chukchi shelf). The model is initialized with a spatially uniform stratification typical of summertime values and forced with a sinusoidally varying wind stress defined as

$$\begin{aligned} \tau^x &= -\tau_m \sin(t\pi/P)\sin\theta\, r/L \qquad \tau^y = \tau_m \sin(t\pi/P)\cos\theta\, r/L \qquad r \leqslant L \\ \tau^x &= -\tau_m \sin(t\pi/P)\sin\theta\, L/r \qquad \tau^y = \tau_m \sin(t\pi/P)\cos\theta\, L/r \qquad r > L \end{aligned} \tag{1}$$

where t is time, P is the duration of the wind event, and θ is the azimuthal angle relative to east. This form of wind stress provides uniform Ekman pumping for $r < L$ and zero Ekman pumping for $r > L$. The parameters are taken to be the same as for the accompanying analytic calculation, $L = 350$ km, the amplitude of the wind stress $\tau_m = 0.04$ N/m^2, and $P = 5$ days. The forcing is centered over the Chukchi shelf, although the region of Ekman pumping extends to the coast of Alaska and across the shelfbreak. The model is initialized at rest and run for 5 days.

3. Mean and seasonal circulation and hydrography of the shelfbreak and slope

3.1. Mean structure

The year-long mean, depth-averaged velocity vectors with standard error ellipses are shown in Fig. 3. This reveals that there is persistent northwestward flow along the Chukchi slope (at CS3, CS4, and CS5), with magnitude much greater than the standard error ellipses. It confirms that the Chukchi Slope Current is a year-round feature, i.e. it is not only present during the summer months as reported in Corlett and Pickart (2017). Note that the vector at CS5 is a bit smaller than that at CS4, which is due to southeastward-directed flow of Atlantic water at depth. The mean vector at CS5 becomes about 1.4 cm/s greater than the vector at CS4 if the average is taken over the Pacific water layer, with instantaneous values approaching 50 cm/s. The mean interface depth between the Pacific water and Atlantic water was calculated using the CMP data following the potential vorticity method of Nikolopoulos et al. (2009). The mean depth was 120 m, 155 m, and 167 m at CS3, CS4, and CS5 with averaging periods of two months, twelve months, and eight months, respectively. There was no presence of Atlantic water at the other five moorings. Progressing onshore past the shelfbreak to the outer-shelf, the mean flow at the next four mooring sites is westward/northwestward. At mooring NE40, however, the flow is directed to the southwest. This is consistent with the notion of anti-cyclonic circulation around Hanna Shoal (e.g. Weingartner et al., 2013; Pickart et al., 2016).

Notably, the depth-averaged flow at mooring CS2 is much weaker than at the other sites; in fact, it is not significantly different than zero. The reason for this can be seen in the mean vertical section of

Table 1
Mooring information.

Mooring ID	Latitude(N)	Longitude(W)	Water Depth(m)	Instrument	Duration	Instrument Depth(m)	Range Depth(m)	Sample Interval(h)	Vertical resolution(m)
FM1	72°15.808′	158°02.463′	67	ADCP	10/25/2013–09/21/2014	60	8–53	1	5
				MicroCAT	10/25/2013–09/21/2014	60	–	0.25	–
CS2	72°18.018′	157°43.522′	102	ADCP	10/12/2013–09/22/2014	89	11–81	1	5
				MicroCAT	10/12/2013–09/22/2014	89	–	0.25	–
CS3	72°20.175′	157°26.893′	163	CMP	10/14/2013–09/21/2014*	–	39–146	6	2
				ADCP	10/13/2013–09/22/2014	151	22–132	1	10
				MicroCAT	10/12/2013–09/22/2014	151	–	0.25	–
CS4	72°23.104′	157°8.762′	249	CMP	10/15/2013–09/21/2014	–	50–235	6	2
				ADCP	10/13/2013–09/22/2014	241	22–222	1	10
				MicroCAT	10/12/2013–09/22/2014	241	–	0.25	–
CS5	72°25.82′	156°50.37′	356	CMP	10/15/2013–06/21/2014	–	42–340	6	2
				ADCP	10/13/2013–09/22/2014	349	31–331	1	10
				MicroCAT	10/13/2013–09/22/2014	349	–	0.25	–
NE40	72°7.345′	160°29.675′	41	ADCP	09/09/2013–09/18/2014	40	3–37	0.5	1
NE50	72°9.731′	159°7.524′	50	ADCP	09/09/2013–09/18/2014	49	4–46	0.5	1
NE60	72°10.892′	158°33.069′	57	ADCP	09/09/2013–09/18/2014	56	5–53	0.5	1

* The CMP at CS3 got stuck near the top of the mooring on December 9, 2013.

alongstream velocity (Fig. 4a). The mean section reveals bottom-intensified southeastward flow at CS2, inshore of the slope current. This demonstrates the year-round presence of the Chukchi Shelfbreak Jet, which was also seen in the summertime mean shipboard section of Corlett and Pickart (2017). Averaged over the year, the Chukchi Slope Current is surface-intensified, confined to depths shallower than 250 m (Fig. 4a). Clearly, the mooring array did not extend far enough offshore to bracket the slope current. In the mean, the maximum flow of the shelfbreak jet is 6 cm/s, while that of the slope current is 13 cm/s. Both the vertical section of Fig. 4a and the summertime mean vertical section of Corlett and Pickart (2017) show southeastward flow of Atlantic water at depth on the mid-slope, which is assumed to be the inshore portion of the Atlantic water boundary current system in the western Arctic.

The mooring hydrographic data captured the different water masses present during the year, which are characterized in the potential temperature-salinity diagram of Fig. 4b. We follow Corlett and Pickart's (2017) definitions of the regional water masses, which in turn are based on earlier studies. We note that the boundaries between the different water types are not precise, in part because they can vary interannually (e.g. Pisareva et al., 2015), but they suffice for our purposes. There were six different water masses measured on the Chukchi shelf and slope over the course of 2013–2014.

Percentage-wise, very little Pacific summer water was present over the shelf and slope. Only a tiny bit of Alaskan Coastal Water was detected in the month of September. This should not be a surprise, however, because nearly all of the Alaskan Coastal Water present in the shipboard sections analyzed by Corlett and Pickart (2017) occurred in the top 40 m, shallower than the hydrographic sensors in our mooring array. Bering summer water was more common. This is a mixture of Anadyr water and central Bering shelf waters (Coachman et al., 1975), and it extends deeper in the water column over the Chukchi slope than the warmer and lighter Alaskan Coastal Water.

The coldest Pacific water is the newly-ventilated Winter Water, which contributes to the local temperature minimum of the Canada Basin halocline (e.g. Steele et al., 2004; Timmermans et al., 2014). This water is formed in the northern Bering Sea (e.g. Muench et al., 1988) and can undergo further transformation as it transits the Chukchi shelf (e.g. Weingartner et al., 1998; Itoh et al., 2012; Pacini et al., 2016). It accounted for 10.6% of the water measured by our array. The second type of cold Pacific water is Remnant Winter Water, which is newly-ventilated Winter Water that has been warmed by a combination of solar heating and mixing (e.g. Gong and Pickart, 2016). This water mass was present throughout the year at the array, accounting for 36.1% of all measurements. The most common water mass observed was the Atlantic Water, with a percentage of 50.3%, located in the deep layer on the slope. Lastly, both early-season (near the freezing point) and late-season Melt Water was detected (Fig. 4b, see Gong and Pickart, 2015).

3.2. Seasonality

The Chukchi Slope Current and Shelfbreak Jet are both present throughout the year (Fig. 5). The former has a pronounced seasonal signal. It is surface-intensified (with a maximum on the order of 20 cm/s at the core) in summer and autumn, and becomes middepth-intensified in winter and spring and moves shoreward with a weaker speed (order 10 cm/s at the core). The monthly-mean sections (not shown) indicate that the mid-depth intensification is present from January to June. By contrast, the shelfbreak jet shows little seasonal variation. It is always bottom-intensified, although it appears to be a bit stronger in fall (maximum velocity of roughly 8 cm/s) and weaker in spring. The southeastward flow of Atlantic water also displays seasonality, with stronger velocity and shallower vertical extent (by roughly 50 m) in fall and winter.

The hydrographic timeseries of potential temperature and salinity at CS4 and CS5 (the two CMPs with the longest records) reveal the

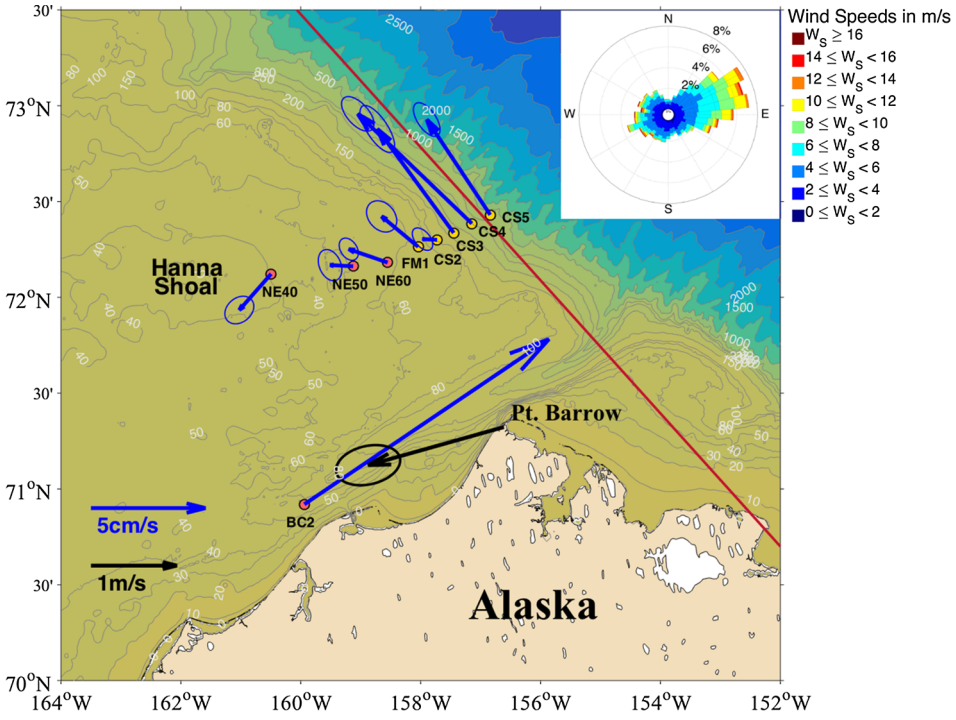

Fig. 3. Year-long, depth-mean velocity vectors (blue) at the mooring sites and mean 10 m-wind vector (black) at the Barrow, AK meteorological station. The standard error ellipses are shown (see the scales at the lower left). The red line indicates the along-stream direction (see Fig. 2b). The wind rose showing wind speed and direction at Barrow for the duration of the deployment is at the upper right. (For interpretation of the references to colour in this figure legend, the reader is referred to the web version of this article.)

seasonality of water masses in the slope current (Fig. 6). The newly-ventilated Winter Water, with temperatures below −1.6 °C, first appeared in March and lasted until the end of August, in the depth range 50–170 m, with a large and continuous amount from early-April to late-July. There is also evidence of local formation of this water mass during the winter months. In particular, there are numerous instances of newly-ventilated Winter Water appearing in the upper 50–75 m from December to February, which is likely the signature of convective overturning driven by brine rejection as a result of re-freezing polynyas. Some warm and fresh water also shows up above 100 m from November to March. At the shelfbreak, the MicroCAT data at the bottom of CS2 indicates that Remnant Winter Water and newly-ventilated Winter Water are two dominant watermasses. Most of the newly-ventilated Winter Water is present from mid-May to mid-September, while Remnant Winter Water is dominant for the remaining time.

The year-long mean wind vector at the Barrow meteorological station is out of the east/northeast (254°T) with a speed of 1.6 m/s (Fig. 3). The wind rose reveals that there were also periods of westerly/southwesterly wind, although they were much less frequent (Fig. 3). Seasonally, the winds were strongest during fall and early winter, and weaker and variable in direction in spring (Fig. 7a). Freeze-up at the mooring site occurred in late November, after which the ice concentration remained above 90% until early July when melting began. The polynya south of Barrow Canyon opened up three times – in early January, late January/early February, and late April/early May – during which times the ice cover was also reduced at the mooring site (Fig. 7b). These periods were preceded by significant northeasterly winds lasting several days (Fig. 7a).

3.3. Dominant modes of velocity

Empirical orthogonal functions (EOFs) were used to determine the dominant variability of the alongstream velocity over the shelfbreak and slope (Fig. 8a–d). The first two modes explain 62.4% and 10.8% of the total variance, respectively. The spatial pattern of mode 1 consists of same-signed values over the entire section. To visualize the associated velocity structure, we added the product of the spatial pattern of mode 1 and positive/negative one standard deviation of the corresponding principal component (PC1) to the year-long mean section. In the former case the slope current is strong and occupies most of the section, with only a weak signature of the eastward-flowing shelfbreak jet (Fig. 8e). In the latter situation the shelfbreak jet is strong, as is the eastward flow of Atlantic water at depth. In this case the slope current is displaced off shore and weakened (Fig. 8g).

The PC1 timeseries fluctuates frequently between positive and negative values, indicating that both states are common. We applied Singular Spectrum Analysis (SSA; see Ghil et al., 2002) to the timeseries in order to characterize the dominant variability. First, we embedded the timeseries into a trajectory matrix with a window length of L, then decomposed the matrix to statistically independent components and reconstructed the dominant ones. We took L to be 10% of the timeseries length, which is long enough to obtain the significantly independent components while under the limit of half of the timeseries length (Hassani, 2007). The SSA curve is shown in Fig. 8c (thick dashed line), indicating that the dominant variability indeed corresponds to frequently occurring fluctuations.

The spatial pattern of EOF mode 2 shows a dipole structure with positive values onshore of $y = 175$ km and negative values offshore (Fig. 8b). Note that the corresponding PC2 timeseries has a different character than the PC1 timeseries, in that it contains longer-term variability. This is quantified by the SSA reconstruction for this mode, which is negative in the cold months of the year and positive in summer/early-fall (Fig. 8d). We added the product of the spatial pattern of mode 2 and the maximum/minimum values of the SSA back into the mean, which are shown in Fig. 8f and h. One sees that this mode reflects lateral shifts of the slope current. In the first instance the slope current is offshore, surface-intensified, and strong. In the second condition it is onshore, middepth-intensified, and weak (the shelfbreak jet is present in both scenarios). These two states correspond to the seasonal configurations presented above (Fig. 5), in both structure and timing. Hence mode 1 is reflective of higher frequency variability, while mode 2 represents the seasonal signal.

We also investigated the possible presence of topographic wave energy in our mooring timeseries. Topographic Rossby waves are commonly found in regions of sloping topography, such as along the mid-Atlantic Bight of the North Atlantic (Johns and Watts, 1986), along

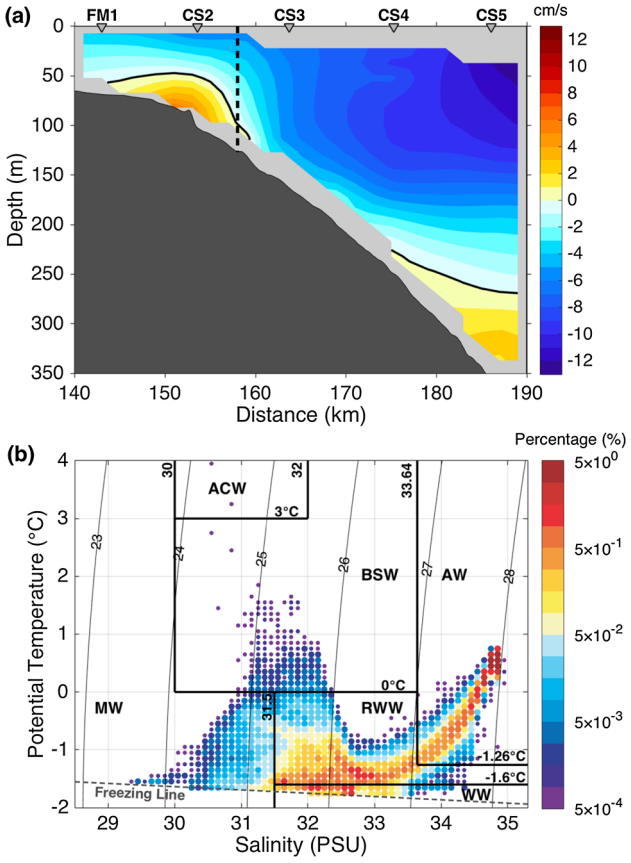

Fig. 4. (a) Year-long mean alongstream velocity section (positive flow is southeastward). The thick black line is the zero velocity contour. The dashed black line shows the boundary between the shelfbreak region and the continental slope. The grey shading indicates regions of no data coverage. The mooring sites are indicated along the top of the plot. (b) Potential temperature-Salinity diagram for all of the hydrographic data. The color represents the percentage of data within a 0.1 °C by 0.1 salinity grid. The thick black lines delimit the different water masses considered in the study: MW = Melt Water; ACW = Alaskan Coastal Water; BSW = Bering Summer Water; RWW = Remnant Winter Water; WW = newly-ventilated Winter Water; AW = Atlantic Water.

the western boundary of the Labrador Sea (Fischer et al., 2015), and along the northwest slope of Iceland (Harden and Pickart, 2018). Two prominent signatures of these waves are that the variance ellipses are skewed relative to the local topography, and there is cross-slope phase propagation of velocity variability (which would not be identified by an EOF). Neither of these signatures are present in our data. The variance ellipses are aligned with the mean flow (which, for geostrophic flow, follows the isobaths), and there is no persistent signature of cross-slope propagation. This further highlights the dominant nature of the variability revealed by our EOF analysis.

4. Volume transport

To estimate the volume transport of slope current and shelfbreak jet, we chose $y = 158$ km as the dividing line between the shelfbreak and slope regions based on the velocity distribution of the year-long mean section (dashed line in Fig. 4a). The transport of the shelfbreak jet, covering the region 140 km $< y <$ 158 km over the full depth of the water column, can be positive (eastward) or negative (westward). We also consider the near-bottom portion flow defined by the region of eastward transport in the mean section (referred to as the bottom shelfbreak jet). For the slope current we consider only the westward flow, so by definition the transport is always negative. The vertical sections of velocity are extrapolated to the surface and to the bottom for the transport computations.

Only 38% of the vertical sections bracketed the main part of slope current. As such, any estimate of transport of the current will be an under-estimate. To help alleviate this, we invoked a "mirroring" technique to estimate the missing transport. For 47% of the sections, the velocity core of the slope current was close to or beyond the edge of the grid. In these cases we took the offshore part of the current to be the mirror image of the inshore part. This was only done using information within 10 km of the edge of the grid, and was also limited vertically to the upper 150 m of the water column (i.e. the strongest part of the flow). In certain sections this approach was not feasible (for example the slope current occasionally had two cores). Of course, there is no *a priori* reason why the slope current should be symmetric as such, but we feel that this was a worthwhile attempt to boost the transport estimate to be closer to the true value, although this estimate is still clearly an underestimate. For the remaining 15% of the sections there was either missing data (10%) or no signature of the slope current (5%). In the former case transport timeseries was interpolated, in the latter case no value was calculated.

The resulting volume transport timeseries and monthly mean transport of the slope current and shelfbreak jet are shown in Fig. 9. The year-long mean westward transport of the slope current is 0.71 ± 0.05 Sv. Using the mean boundary between the Pacific water and Atlantic water (see Section 3.1 above), the year-long mean transport of Pacific water is 0.57 ± 0.04 Sv. This value includes the contribution due to melt water in the upper layer. The collection of shipboard sections used by Corlett and Pickart (2017) extended to the surface, hence they were able to compute the westward transport of melt water by the slope current for the period July-October, which was estimated to be 0.19 Sv (B. Corlett, pers. comm., 2017). Assuming that there is negligible transport of this water mass during the remaining months of the year, this implies a yearly averaged melt water transport of 0.06 Sv. Subtracting this from our mean value gives 0.51 Sv. This is line with Corlett and Pickart's (2017) estimate of 0.50 ± 0.07 Sv. Included in Fig. 9a are synoptic estimates of the slope current Pacific water transport from eight shipboard sections conducted during the mooring year. These agree reasonably well with the timeseries values determined from the moorings (cyan curve). The transport of the slope current varies substantially on a variety of time scales, ranging from near zero to 2 Sv (Fig. 9a).

The year-long mean transport in the vicinity of shelfbreak is also westward, 0.025 ± 0.008 Sv. The flow fluctuates between positive and negative throughout the year (grey curve in Fig. 9b), with a range of approximately −0.2 to 0.2 Sv. However, as seen in Fig. 4a, the eastward-flowing shelfbreak jet is bottom-intensified. Considering the near-bottom portion only (red curve in Fig. 9b), the year-long mean transport is 0.009 ± 0.003 Sv to the east. This value is smaller than the transport of the Beaufort shelfbreak jet measured in recent years (mean of 0.023 ± 0.018 Sv to the east, from 2008 to 2014; P. Lin, pers. comm., 2017).

The monthly mean timeseries indicates that the transport of the slope current is larger in summer, with a peak value in September (Fig. 9c). This is slightly at odds with the results of Corlett and Pickart (2017) who found that the slope water transport was largest in October, although they computed the transport for different time periods. The monthly-averaged transport of the flow at the shelfbreak is westward from December to July and eastward for the other months except September. The transport within the near-bottom region of the shelfbreak is eastward for all months except May and June. Recall that there is no Atlantic water present at the bottom of CS2, so the transport computed here is all Pacific water transport.

The transport timeseries of the slope current and the shelfbreak jet have a significant negative correlation after removing the high-frequency fluctuations. The correlation coefficient is −0.6 at a confidence level of 95% using 5-day low-pass filter on both timeseries. This relationship is explored further in the next section.

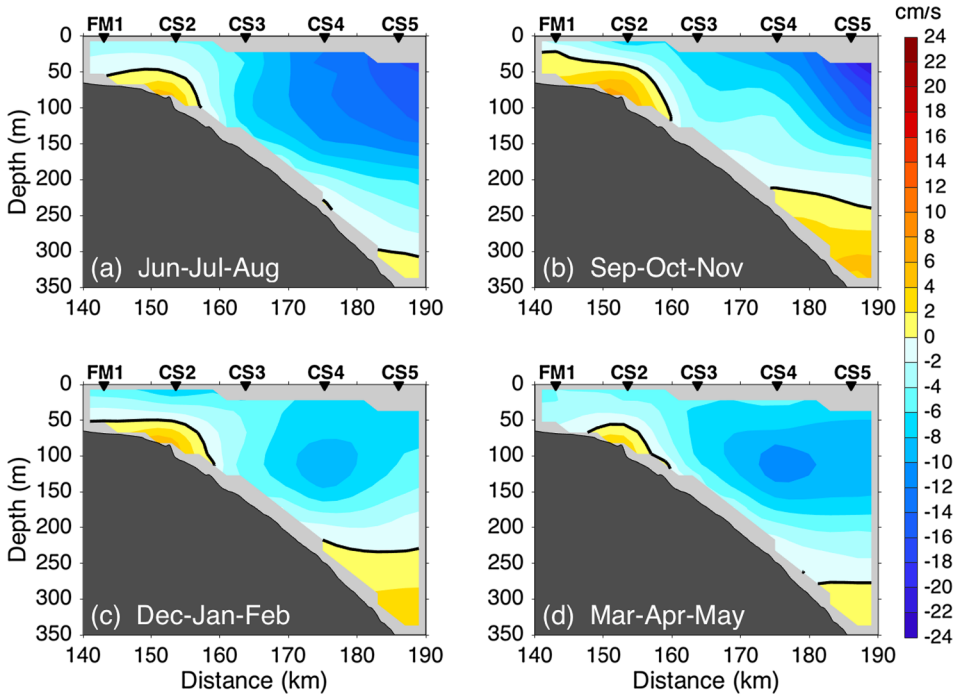

Fig. 5. Vertical sections of the seasonally averaged alongstream velocity. The presentation is the same as in Fig. 4a.

5. Extreme states of the slope current and shelfbreak jet

Recall that the positive/negative states of EOF mode 1 (the dominant mode) for the alongstream velocity are (1) a strong slope current and weak-to-no shelfbreak jet; and (2) a weak slope current that is displaced offshore, with a very strong eastward-flowing shelfbreak jet. This result, together with the negative correlation in transport of the two currents, motivates us to elucidate this relationship and try to understand what drives this variability.

Corlett and Pickart (2017) argued that the westward flow of the Chukchi Slope Current is enhanced under strong easterly winds (exceeding 4 m/s) along the shelfbreak for the months of July-October (the seasonal time period of their study). The easterly direction was taken to be the component of wind directed from the southeast parallel to the shelfbreak. In an attempt to corroborate their result, we did the same exercise using the mooring data for the same months of the year, and obtained a similar result, i.e., an enhanced slope current and a weaker shelfbreak jet.

To expand on this analysis and include the full year, we isolated all the times when the slope current was strong while the shelfbreak jet was simultaneously reversed to the west, as well as those times when the shelfbreak jet was flowing strongly to the east while the slope current was weak. The criteria used for the first type of event was that the slope current transport be at least 0.3 standard deviations greater than the mean, while the flow at the shelfbreak be at least 0.3 standard deviations weaker (more negative) than the mean. For the second condition, the shelfbreak jet had to be at least 0.3 standard deviations larger (more positive) than the mean, while the slope current needed to be at least 0.3 standard deviations weaker than the mean. We further divided the events by the quadrant from which the wind was blowing.

The event statistics are summarized in Table 2. Overall, the strong slope current/weak shelfbreak jet condition occurred ~16% of the time, while the weak slope current / strong shelfbreak jet scenario occurred ~18% of the time. We chose to focus on these extreme states to maximize the relationships between the oceanographic and atmospheric signals. The results are not overly sensitive to the precise fraction of the standard deviation chosen to define the events. We also did not consider any events shorter than 12 h in duration, and two events are considered one if the time gap between them is less than 12 h. The occurrences of the two types of conditions are marked in Fig. 8c in relation to the principal component timeseries of EOF 1. One sees that the peaks of PC1 are consistent with the periods of the two states.

5.1. Strong slope current and reversed shelfbreak jet

Based on the results of Corlett and Pickart (2017), one might expect these conditions to always correspond to an easterly wind (i.e. with a component of the wind paralleling the shelfbreak from the southeast). Surprisingly, however, this extreme state occurred under various wind conditions (Table 2). Here we consider the two wind conditions that resulted in the most days with a strong slope current and reversed shelfbreak jet: southwesterly and northeasterly directed winds, which together account for more than 78% of the total duration of this state (Table 2).

5.1.1. Winds from the southwest

There were 15 instances in which the slope current was anomalously strong and the shelfbreak jet was reversed while the wind was from the southwest. The composite mean vertical section of alongstream velocity (Fig. 10a) shows that there was westward flow throughout the array, with the slope current 5–10 cm/s stronger than normal (Fig. 10b). Low sea level pressure (SLP) was present in the southern Canada Basin, with associated cyclonic winds (Fig. 10c), while higher SLP was present to the south (with a maximum in the Bering Sea, not shown). The wind stress curl was strongly positive on the northeastern Chukchi shelf (Fig. 10d), producing divergent conditions for Ekman transport. This implies that there would be a drop in sea surface height on the shelf, which would set up a geostrophic response of enhanced flow to the west along the Chukchi shelfbreak/slope, consistent with the mooring observations.

5.1.2. Winds from the northeast

The second most common occurrence of this extreme state occurred when the wind was out of the northeast, with a total of 9 events. As with the previous situation, the alongstream velocity was strongly northwestward across the array (Fig. 11a), with the maximum velocity anomaly somewhat larger and located deeper in the water column (Fig. 11b). In contrast to the previous case, high SLP was present in the northern Beaufort Sea (Fig. 11c) and low SLP farther to the south.

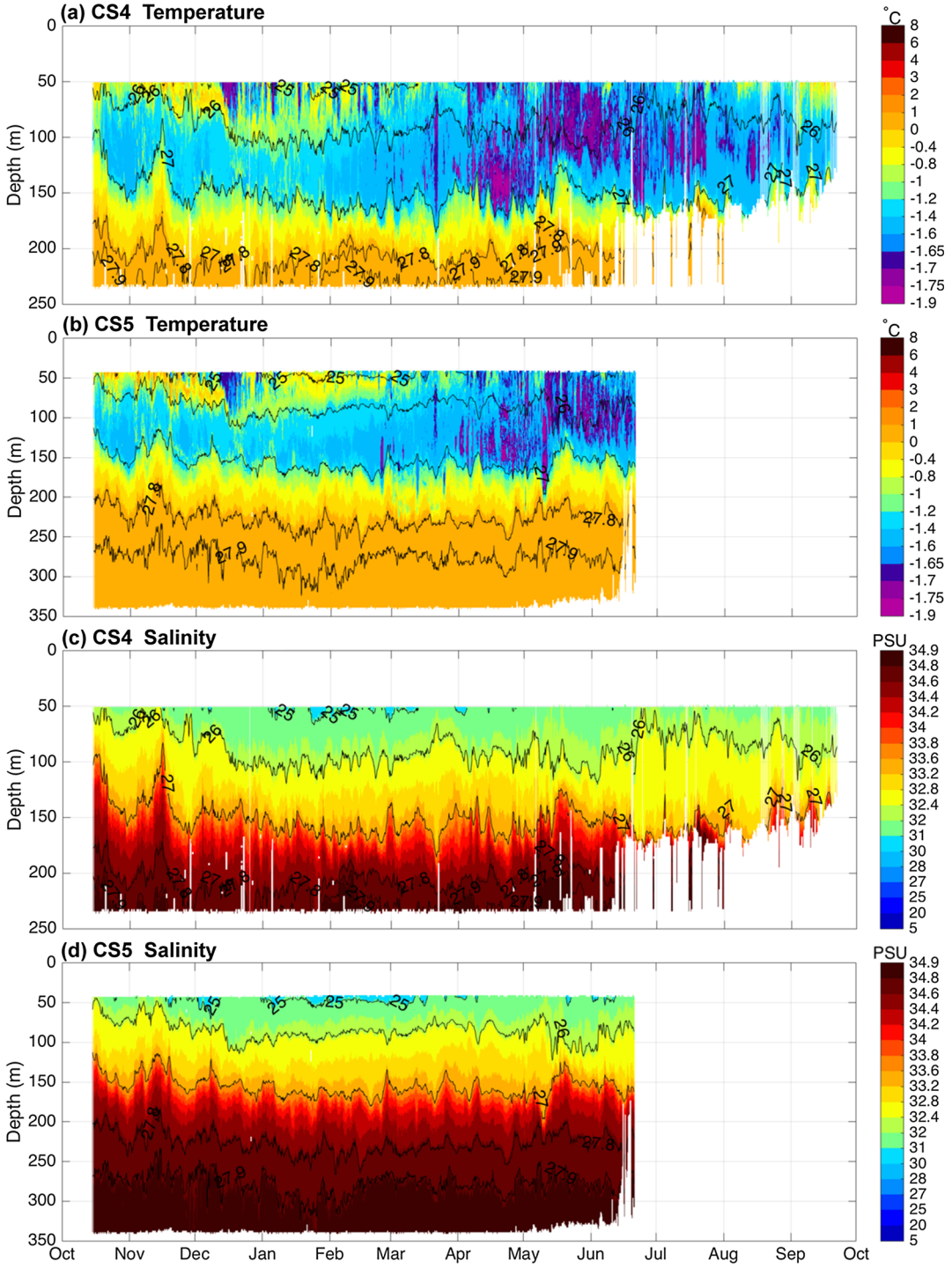

Fig. 6. Depth-time plot of potential temperature and salinity (color) at CS4 (a, c) and CS5 (b, d), overlain by potential density (contours, kg m^{-3}).

However, despite this difference in the atmospheric circulation, the wind stress curl was again positive on the northeastern Chukchi shelf (although not as strong as in the previous condition, Fig. 11d), conducive for increased westward flow along the Chukchi shelfbreak/slope via geostrophic set up.

5.2. Strong shelfbreak jet and weak slope current

5.2.1. Winds from the northeast

Unlike the previous extreme state, which had roughly equal percent occurrences for southwesterly and northeasterly winds, the opposite extreme of a strong eastward-flowing shelfbreak jet and weak slope current was predominantly due to a single wind condition, that of northeasterly winds (Table 2). There were a total of 22 such events. The composite alongstream velocity section shows that the shelfbreak jet was ~10 cm/s near the bottom, with southeastward flow all along the continental slope transporting Atlantic water at depth (Fig. 12a). The slope current was significantly weaker than in the mean, with a maximum anomaly of ~10 cm/s between 75 and 200 m depth (Fig. 12b). The atmospheric pattern associated with this state consists of high SLP in the Canada Basin and lower SLP to the south (Fig. 12c). The corresponding circulation results in strongly negative wind stress curl on the

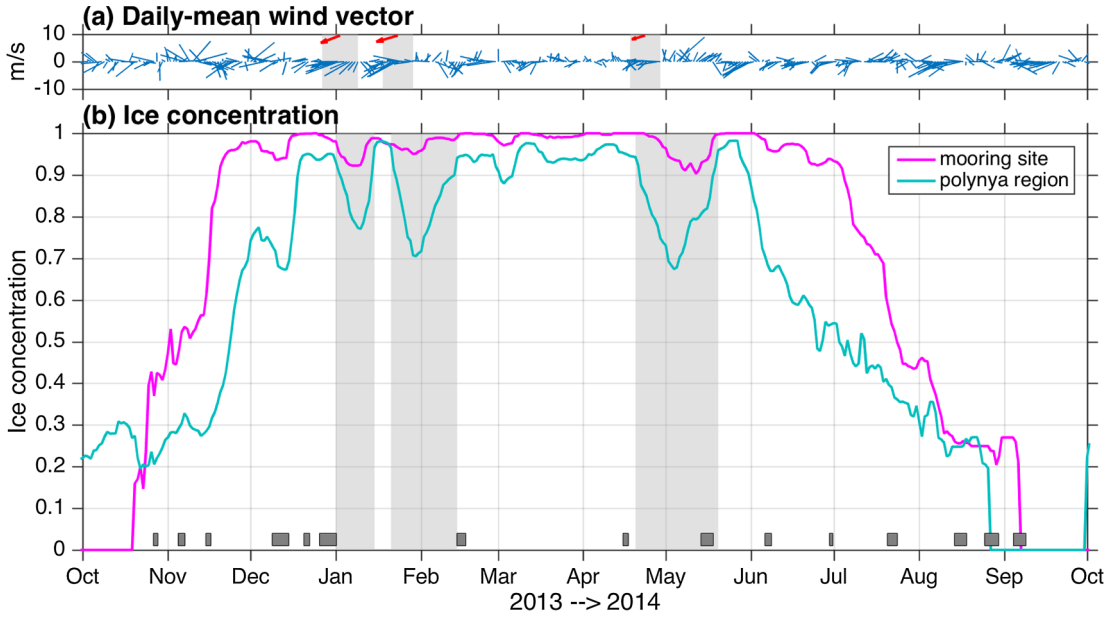

Fig. 7. (a) Daily-mean wind velocity at the Barrow meteorological station (blue vectors). The light gray shading and red vectors denote periods of northeasterly wind, and the corresponding mean wind velocity, preceding the three major occurrences of reduced ice cover at the mooring array site and south of Barrow Canyon. (b) Ice concentration timeseries at the array site (magenta curve) and at the location of the polynya south of Barrow Canyon (cyan curve). The light gray shading indicates the three periods of reduced ice concentration. The dark grey segments at the bottom of the plot indicate when upwelling occurred. (For interpretation of the references to colour in this figure legend, the reader is referred to the web version of this article.)

northern Chukchi shelf (Fig. 12d), which would lead to Ekman convergence and a rise in the sea level height. This in turn would cause enhanced southeastward flow along the Chukchi shelfbreak/slope as observed.

This situation is consistent with results from a previous study of a storm event in this region. Pickart et al. (2011) analyzed the response of the northeast Chukchi Sea and western Beaufort Sea to a strong Aleutian Low, using both observations and a regional numerical model. The cyclone resulted in northeasterly winds over a three-day period similar to that seen in Fig. 12c. Mooring data on the Chukchi slope, roughly 300 km to the west of our mooring array, showed a stronger eastward-flowing Chukchi Shelfbreak Jet during the storm. The model indicated that this arose due to an increase in sea level on the Chukchi shelf associated with strong negative wind stress curl and Ekman convergence. This lends credence to our interpretation of these extreme events seen in our data.

5.3. Dynamical considerations

5.3.1. Observed phase relationship of forcing and response

The above analysis implies that the wind stress curl plays a key role in the occurrence of the extreme states. To examine this further, we diagnosed the timing of the two types of events to quantify the relationship between the wind stress curl and oceanographic response. First, we normalized the time of each individual event for all of the strong slope current / reversed shelfbreak jet cases and all of the weak slope current / strong shelfbreak jet cases. Time zero/one was the start/end of the event based on the mooring velocity records, and we extended the temporal domain on either side of the event by one time unit to include the spin up and spin down. The wind stress curl was averaged spatially within the area marked on Fig. 10d, 11d, and 12d, and this signal, as well as the transport signals, was low-passed with a 3-day filter width prior to isolating the events and normalizing in time to remove high-frequency noise. The individual events for the two extreme states were then averaged together to obtain a composite time evolution for each.

The results of this calculation are shown in Fig. 13. The top row is the strong slope current / reversed shelfbreak jet case, and the bottom row is the weak slope current / strong shelfbreak jet case. In the former case the westward transport of the slope current increases from 0.65 Sv prior to the event to 1.2 Sv during the event, dropping to 0.7 Sv after that. The shelfbreak jet transport goes from about 0.05 Sv to more than 0.1 Sv to the west (the transport here is that of the entire shelfbreak region, not just the bottom portion). There is a phase lag between the peak of the wind stress curl and the peak of the volume transports of about 0.2, which corresponds to 17 h in the mean. Such a lag is seen in the individual events as well (with a range of 10 h to 1.9 days).

The composite timeseries for the latter case show an analogous situation (bottom row of Fig. 13). The westward transport of the slope current decreases from about 0.7 Sv before the event to 0.3 Sv during the event, increasing back to the original value afterwards. At the same time the shelfbreak jet transport becomes positive, reaching a value of 0.05 Sv. The wind stress curl signal is roughly the opposite of the former case, becoming strongly negative. Again there is a phase lag between the wind stress curl and volume transports, with the curl leading by 0.25, corresponding to 18 h in the mean. The individual events generally show this pattern as well, but with more scatter than the other type of event (a range of 0 h to 5.9 days).

These composites imply a clear relationship between the wind stress curl on the Chukchi shelf and the transport of the two currents north of the shelf. The next question is, does the observed phase lag between the forcing and response, as well as the magnitude of the response, make sense dynamically?

5.3.2. Theoretical model

A simple theory was derived to shed light on the oceanic response to wind stress curl over the Chukchi shelf. The purpose is not to reproduce the observations in detail, but instead provide insight into the general behavior and to identify the key parameters that control the lowest order response to a region of cyclonic or anti-cyclonic wind stress curl over the shelf. Consider a region of the shelf subject to wind stress curl (Fig. 14). For simplicity, it is assumed that there is uniform Ekman pumping over a circular region of radius L and depth H. The velocity U along the perimeter of this region scales with the gradient of sea surface height, through geostrophy, as $U = g\eta/f_0 L$, where η is the sea surface height anomaly in the center of the domain, g is the gravitational acceleration, and f_0 is the Coriolis parameter. A region of anti-cyclonic wind stress curl, as depicted in the figure, will force a convergence of the Ekman transport, a doming of the sea surface, and a downward

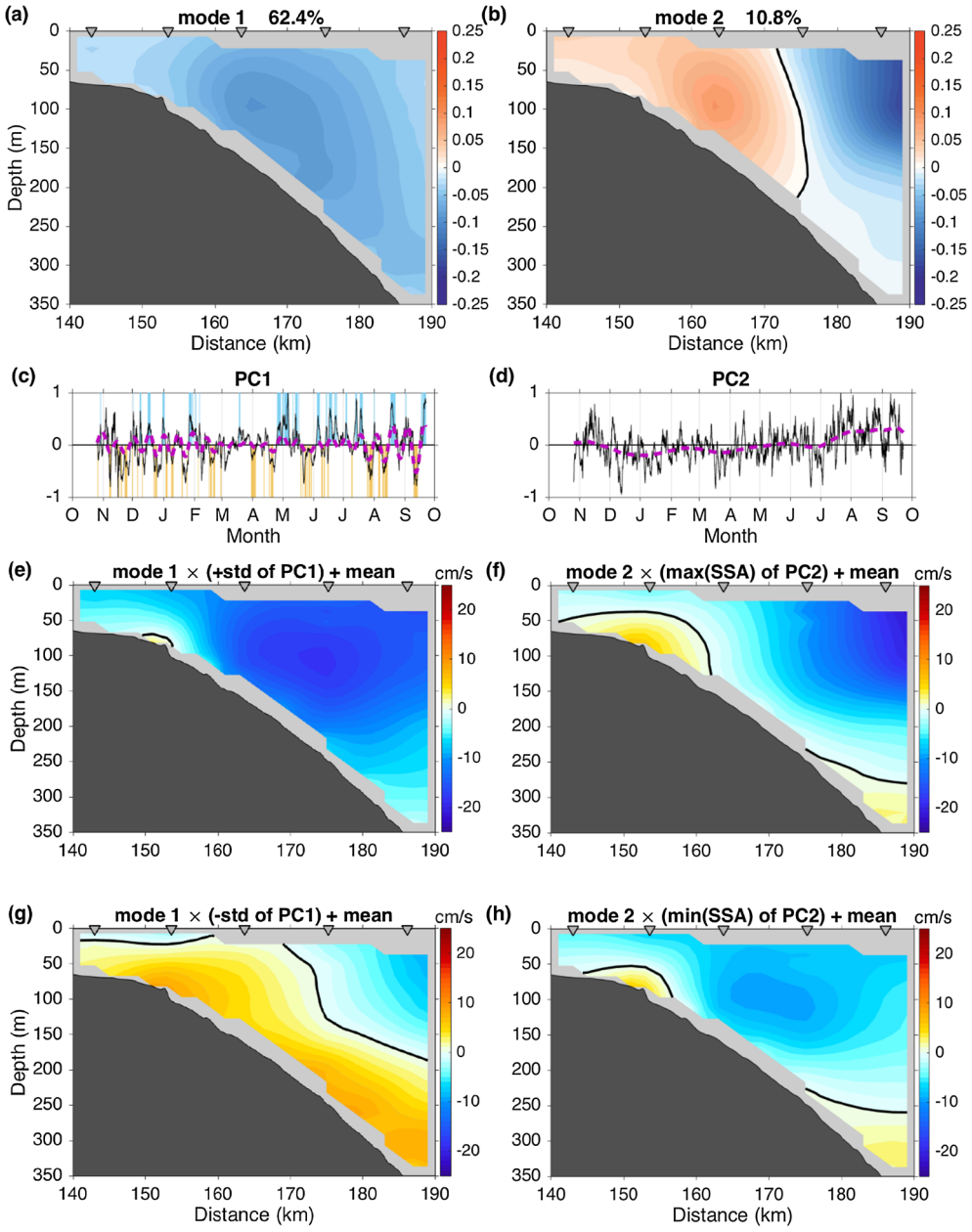

Fig. 8. The first two EOF modes associated with the alongstream velocity sections. The left-hand column is mode 1 and the right-hand column is mode 2. (a,b) Spatial structure of the modes, including the percent variance explained by each. (c,d) The principal component timeseries of each mode. Note that the values are normalized to a maximum of 1. The dashed purple lines are the reconstructed SSA curves. The blue and yellow shaded regions in (c) denote the realizations of the two different states considered in Section 5 (see text). (e,g) Mode 1 multiplied by positive/negative one standard deviation of PC1, added to the year-long mean section. (f,h) Mode 2 multiplied by the maximum/minimum SSA value for PC2, added to the year-long mean section. (For interpretation of the references to colour in this figure legend, the reader is referred to the web version of this article.)

Ekman pumping. Because the perimeter of the circle is closed and the flow is on an $f-$plane, the geostrophic flow across the perimeter is exactly zero. The net inflow in the surface Ekman layer must be balanced by an ageostrophic horizontal velocity, which we assume takes place in a bottom boundary layer. As the sea surface height grows, a lateral pressure gradient develops that drives an anti-cyclonic flow. This acceleration will continue until the export in the bottom boundary layer matches the inflow in the surface Ekman layer. It is implicitly assumed that there is a vertical separation between the surface and bottom boundary layers. For time-dependent forcing there can be a lag between the surface and bottom Ekman layers, leading to a lagged evolution of the sea surface height and horizontal circulation relative to the wind forcing.

This mass budget results in a simple equation for the evolution of η as

$$\frac{\partial \eta}{\partial t} = w_E - \frac{2C_d g \eta}{f_0^2 L^2}, \tag{2}$$

where w_E is the Ekman pumping velocity and C_d is the bottom drag. Similar, but more complicated, approaches have been applied by Nöst and Isachsen (2003), Isachsen et al. (2003), and Spall (2016). Given that the wind events in the Chukchi Sea region demonstrate a clear beginning, peak, and end, we will represent the Ekman pumping by a simple sinusoidal forcing with maximum amplitude W_E and period $2\pi/\omega$, $w_E = W_E \sin(\omega t)$, and consider solutions for $0 < t < \pi/\omega$, i.e. a single pulse of wind with a peak Ekman pumping of W_E.

For an initial condition of $\eta = 0$, the solution to (2) is

$$\eta = \frac{W_E \lambda \gamma \sin(\omega t - \varphi)}{(1 + \lambda^2\gamma^2\omega^2)^{1/2}} + \frac{W_E \lambda^2 \gamma^2 \omega}{1 + \lambda^2\gamma^2\omega^2} e^{-t/\lambda\gamma}, \tag{3}$$

where the non-dimensional constant $\lambda = L^2 f_0^2 / gH$ is the square of the ratio of the length scale of forcing L to the barotropic deformation radius, and $\gamma = H/2C_d$ is the Ekman spin-down time. The spatial scale of the forcing is important because the total Ekman pumping increases as L^2 while the export in the bottom boundary layer increases only as L, so large L results in a stronger circulation. Typical parameters for the Chukchi Sea are $H = 40$ m, $L = 350$ km, and $\lambda = 4.4$. For a typical bottom drag of 10^{-3}m/s, $\gamma = 2 \times 10^4$s. This is shorter than the time

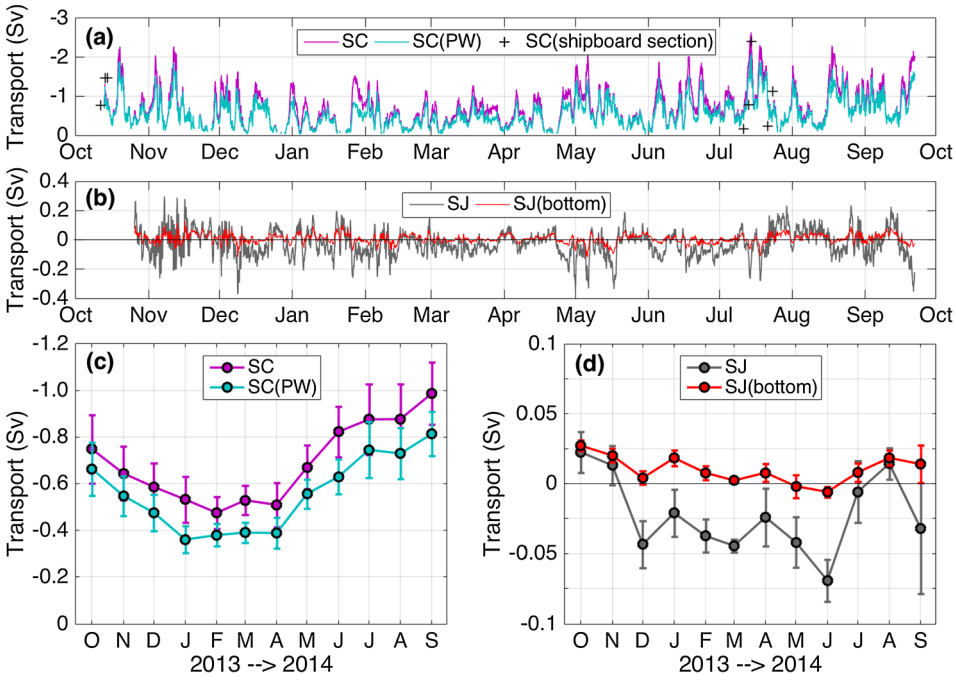

Fig. 9. Volume transport timeseries of (a) the Chukchi Slope Current (purple curve), Pacific water in the Chukchi Slope Current (cyan curve), Pacific water in the Chukchi Slope Current from eight shipboard sections occupied during the year (black crosses), and (b) the Chukchi Shelfbreak Jet (grey curve) and bottom portion of the shelfbreak jet (red curve, see text for explanation). (c) Monthly-mean slope current transport with standard errors. (d) Monthly-mean transport and standard errors for the shelfbreak jet (grey curve) and bottom portion of the shelfbreak jet (red curve). The Pacific water transports include the melt water contribution. (For interpretation of the references to colour in this figure legend, the reader is referred to the web version of this article.)

Table 2
Statistics for the two types of extreme events considered in the text: (i) strong slope current and reversed shelfbreak jet; (ii) strong shelfbreak jet and weak slope current. The first column indicates the quadrant from which the wind was blowing. The percentage in parentheses corresponds to the fraction of the event length relative to the total length in the last row. The underlined percentages represent the fraction of total length relative to the year-long duration of the record. The three primary scenarios considered in the text are in bold.

	Strong SC & reversed SJ			Strong SJ & weak SC		
	Number of events	Total length in days	Mean event length in days (range)	Number of events	Total length in days	Mean event length in days (range)
SW-wind	**15**	**23.1 (42.4%)**	**1.5 (0.5 ~ 4.6)**	3	3.3 (5.4%)	1.1 (0.7 ~ 1.8)
NE-wind	**9**	**19.5 (35.7%)**	**2.2 (0.8 ~ 3.8)**	**22**	**36.1 (60.0%)**	**1.6 (0.6 ~ 4.3)**
SE-wind	3	9.4 (17.2%)	3.1 (1.3 ~ 5.1)	7	12.3 (20.3%)	1.8 (0.6 ~ 5.0)
NW-wind	2	2.6 (4.7%)	1.3 (1.1 ~ 1.5)	7	8.6 (14.3%)	1.2 (0.5 ~ 2.1)
Total	29	55 (15.8%)	1.9	39	60 (17.5%)	1.5

scale for synoptic weather events in the region, so $\gamma\omega < O(1)$ and friction is expected to be important.

Eq. (3) was integrated subject to an average 5-day wind event with a peak wind stress of 0.04 N/m^2 (Fig. 15). This corresponds to a wind stress curl of O(1 × 10^{-7} N/m^3), in line with the observed forcing in Fig. 13a,d. The duration of 5 days is consistent with the wind anomaly preceding and extending past the defined velocity anomaly, which has a typical duration of 3.5 days. The sea surface height grows over several days, peaking near 0.15 m about 21 h after the peak in wind stress. The transport peaks at the same time at about 0.47 Sv, close to the measured increase in the slope current transport (0.4–0.6 Sv, Fig. 13b,e). To demonstrate the importance of bottom drag, the sea surface height for $C_d = 0$ ($\gamma = \infty$) is indicated by the dash-dot line. It peaks at the end of the wind event (since it is simply an accumulation of the Ekman transport) with an amplitude about four times that found with typical bottom friction. The transport would see a similar increase in magnitude and be found to be a maximum at the end of the forcing. These results compare favorably, both in amplitude and phase, to the average wind-forced event described above (Fig. 13). Because the system is linear, a cyclonic wind stress of the same magnitude would produce the same response, just of opposite sign.

We note that the presence of pack-ice has been ignored in these calculations. However, using the ice velocity data set described in Section 2.4, we demonstrated that the ice was mobile throughout the year on the Chukchi shelf/slope and it did not impact the patterns of surface stress imparted to the ocean. In particular, we computed daily fields of ice velocity curl, and then made composite averages for the three extreme event cases analyzed above: the strong slope current / reversed shelfbreak jet case with southwesterly and northeasterly winds, and the weak slope current / strong shelfbreak jet case with northeasterly winds. In each instance the pattern of ice curl was the same as the wind stress curl. It is worth noting that there were several events for each scenario when there was no ice present in the study region.

While the above theory provides simple, intuitive closed form solutions, several strong assumptions were required, such as a flat bottom and no stratification. To test the basic predictions under more complete physics and realistic geometry, the regional primitive equation model described in Section 2.5 was run using the same forcing parameters as the above analytic calculation. This model was stratified, used 5 m vertical grid spacing, and has a realistic bottom topography. The transport anomaly driven by the wind stress anomaly over the shelf (Ψ_m) is indicated on Fig. 15 by the bold dashed line. The primitive equation model agrees closely with the prediction from the theory, in both phase and amplitude of the response, providing confidence that the assumptions in the theory do not compromise the basic predictions.

For $\lambda\gamma\omega << 1$, the sea surface height is in phase with the forcing and linearly dependent on $W_E\lambda\gamma$. This corresponds to the small forcing length scale or strong bottom drag limit. Interestingly, in this regime the magnitude of the response is independent of the forcing frequency

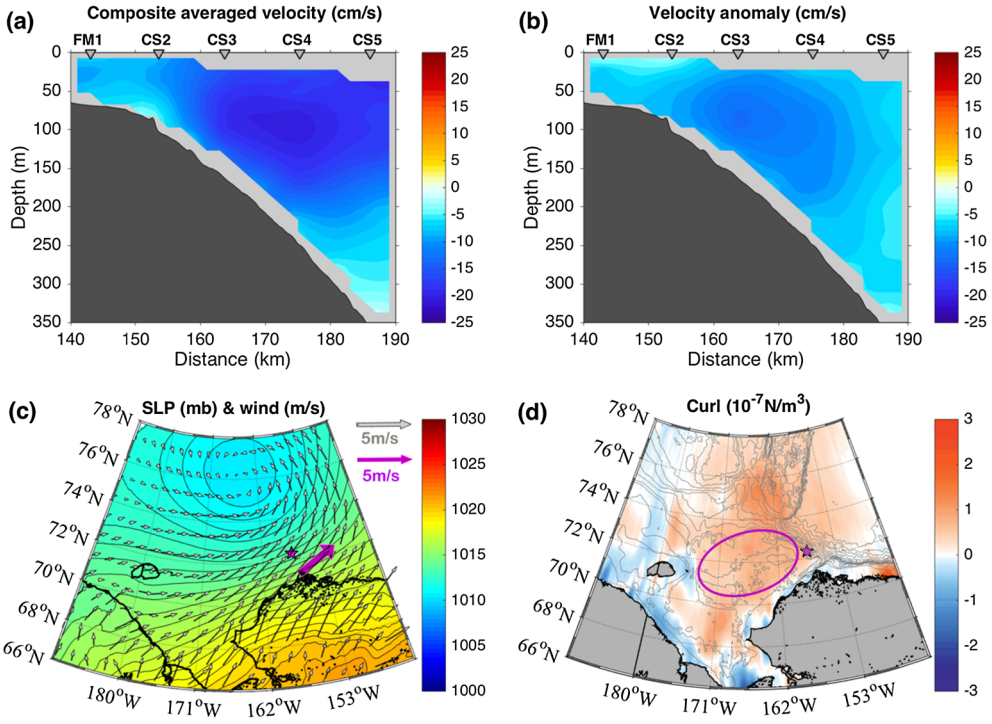

Fig. 10. Composite average fields for the strong slope current/reversed shelfbreak jet events with southwesterly wind. (a) Vertical section of alongstream velocity. (b) Vertical section of alongstream velocity anomaly (composite minus the year-long mean). (c) Sea level pressure (color) and 10 m-wind vectors from NARR (grey vectors), along with the measured wind from the Barrow meteorological station (purple vector). The location of the shelfbreak/slope mooring array is indicated by the purple star. (d) Wind stress curl (color). The purple ellipse indicates the domain that is used to compute the mean wind stress curl on the shelf in Fig. 13. (For interpretation of the references to colour in this figure legend, the reader is referred to the web version of this article.)

(or duration of the storm). In the opposite limit of $\lambda\gamma\omega >> 1$, corresponding to large-scale forcing or weak bottom drag, the sea surface height approaches $2W_E/\omega$ and the phase lags by 90° (the factor of 2 comes from the second term in (3), which is negligible in the limit of small $\lambda\gamma\omega$). In this regime the sea surface height anomaly is larger for longer storms.

6. Upwelling

One of the dominant mechanisms of shelf-basin exchange along the Alaskan Beaufort continental shelfbreak is wind-driven upwelling. This occurs readily for easterly winds exceeding 4 m/s during all seasons of the year (Pickart et al., 2009; Schulze and Pickart, 2012), but not by the local wind stress curl (Lin et al.,2018), the inference being that it is coastal upwelling (the Beaufort shelf is only 50 km wide). While there have been anecdotal reports of upwelling along the Chukchi shelfbreak (e.g. Llinás et al., 2009; Spall et al., 2014), there have been no mooring arrays spanning the Chukchi shelfbreak/slope until now. As such, it is of interest to examine our moorings records for evidence of upwelling. Note that, because the Chukchi shelf is so wide (order 500 km), any

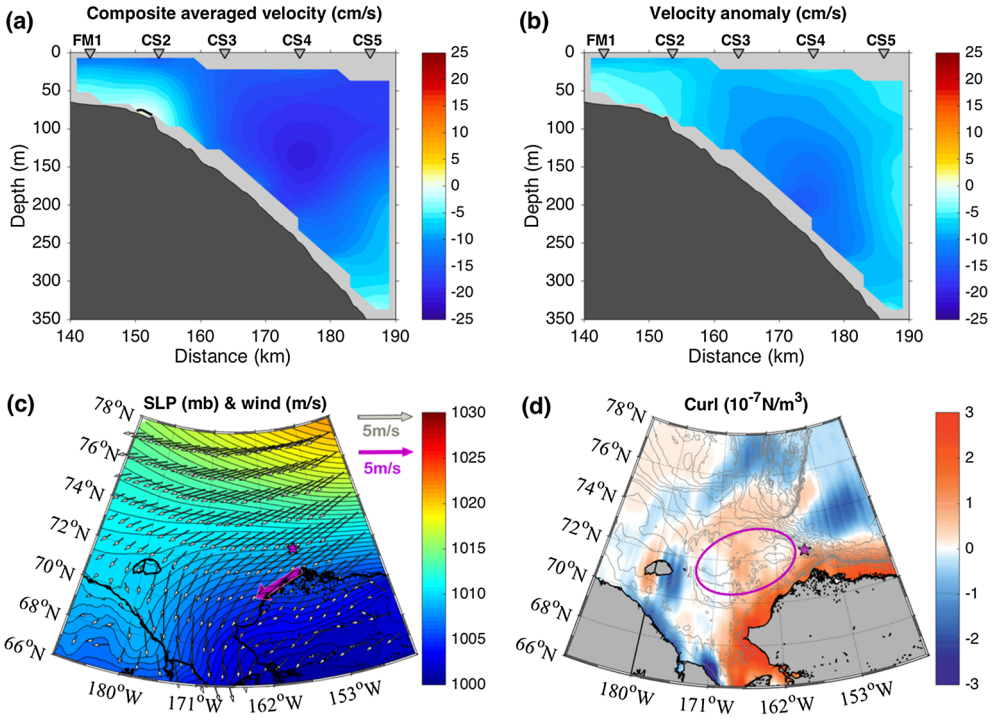

Fig. 11. Same as Fig. 10, except for events with northeasterly wind.

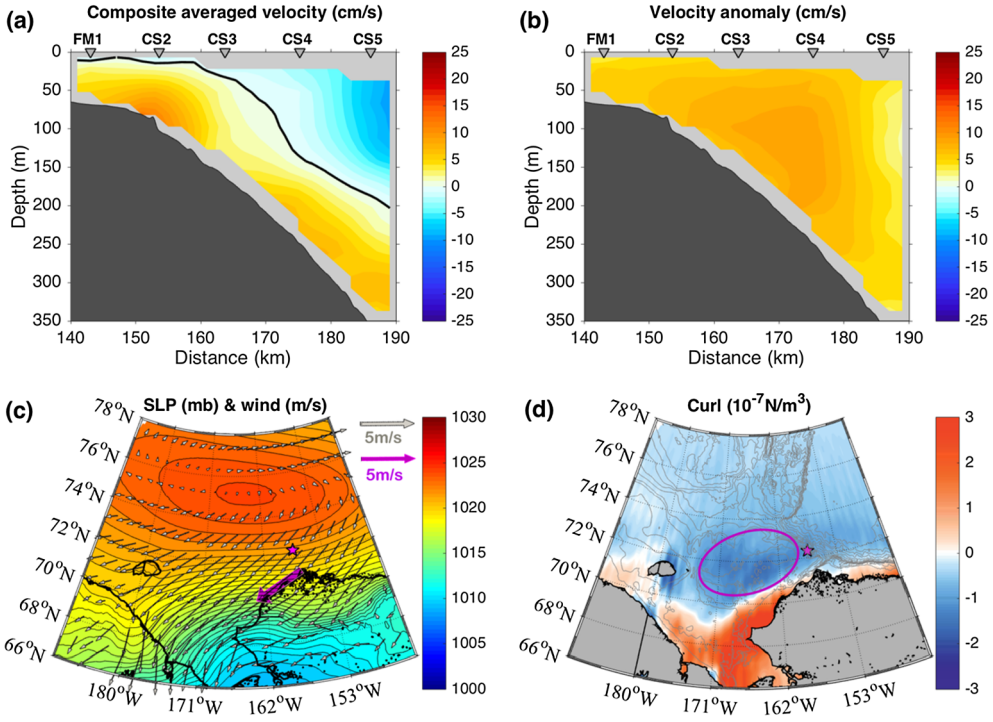

Fig. 12. Same as Fig. 10, except for the strong shelfbreak jet and weak slope current events with northeasterly wind.

such signals would not be due to coastal upwelling.

Following Lin et al. (2018), we use the near-bottom potential density anomaly in the vicinity of the shelfbreak as a metric for the occurrence of upwelling. The density anomaly is computed from the 20-day low-passed MicroCAT potential density records. Upwelling was deemed to occur when the density anomaly at the shelfbreak mooring (CS2) was positive for more than one day, and the density at the outer shelf mooring (FM1) showed a similar increase during the period. If the time gap between two events was less than 12 h, the two events were considered as a single event.

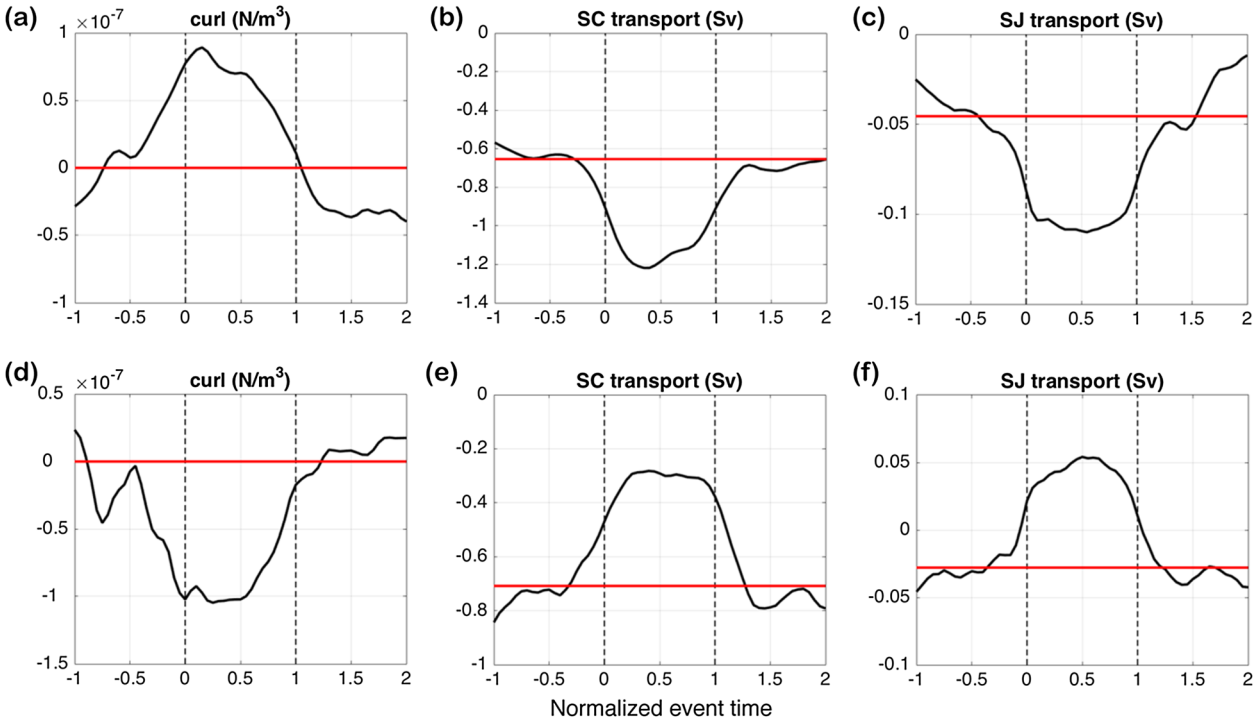

Fig. 13. Normalized timeseries of the two types of extreme events (see text for details). The top row is for the case of a strong slope current/reversed shelfbreak jet. The bottom row is for the case of a weak slope current and strong shelfbreak jet. The first column is wind stress curl averaged over the regions shown in Fig. 10d, 11d, and 12d. The second column is the transport of the Chukchi Slope Current. The third column is the transport of the shelfbreak region. The "SC" and "SJ" denote the slope current and the shelfbreak jet, respectively. The red lines in (a) and (d) show the zero lines and those in other panels show the mean for the normalized time of −1 to 0. The dashed lines mark the duration of the normalized event.

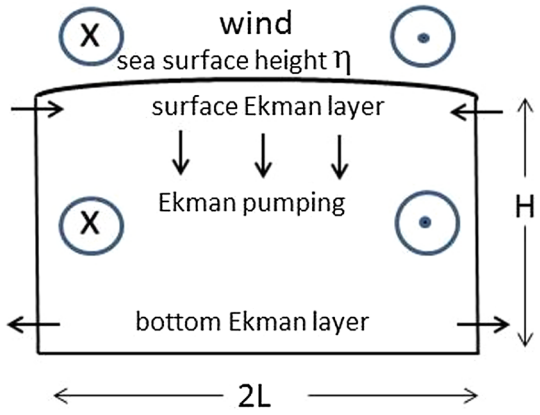

Fig. 14. Schematic of the wind-forced circulation over a circular region of diameter 2*L*.

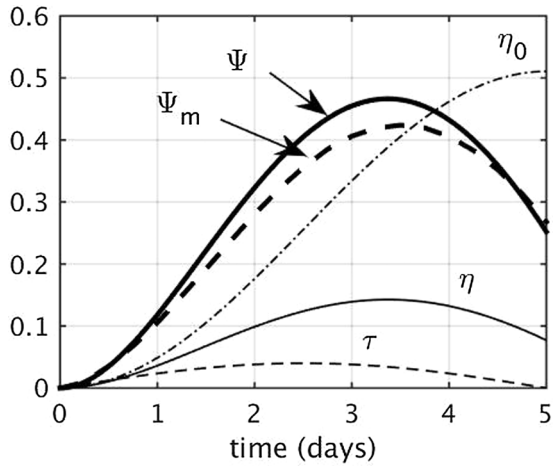

Fig. 15. Sea surface height η(m) for typical parameter values (see text), transport streamfunction (Ψ from theory, Ψ_m from numerical model) (Sv), sea surface height with no bottom drag (η_0), and temporal distribution of wind stress τ(N/m^2).

A total of 15 upwelling events were identified during the year 2013–14 using our criteria. By comparison, Lin et al. (2018) found an average of 22 events per year using a 6-year mooring record at the Alaskan Beaufort shelfbreak. The upwelling identified here occurred in all seasons (dark grey blocks in Fig. 7), which was the case for the Beaufort shelfbreak as well (Schulze and Pickart, 2012; Lin et al., 2018). Following Lin et al. (2018), a measure of the strength of the upwelling, is an index defined as the time integral of the density anomaly over the event's duration. This definition takes into account both the duration and magnitude of the event. Upwelling occurrence statistics are shown in Table 3.

The upwelling event lengths varied from 1.3 days (event 11) to 6.2 days (event 6), with a mean length of 3.5 days. This is shorter than the upwelling events observed on the Beaufort shelfbreak, which averaged 4.8 days based on 6 years of mooring data (P. Lin, pers. comm., 2017). The upwelling index ranges from 1.1 kg m^{-3}h (event 5) to 26.7 kg m^{-3}h (event 9), with a mean value of 5.9 kg m^{-3}h, also smaller than that for the Beaufort Sea. Hence, upwelling events on the Chukchi slope appears weaker than those on the Beaufort slope.

There are no clear trends relating the nature of the atmospheric forcing to the occurrence of upwelling at our array site. The winds are from different directions and the local wind stress curl varies in sign from event to event. As such, neither easterly wind nor positive local wind stress curl – two likely forcing mechanisms – are required for upwelling to occur. Of the 15 events, 7 occurred during partial ice cover (concentrations less than 70%) and the other 8 events occurred during heavy ice (concentrations greater than 90%). There was no correlation between the strength of the upwelling and the ice concentration, in contrast to the Beaufort Sea where the upwelling is strongest during the partial ice season and weakest during the full ice season (Schulze and Pickart, 2012). Both the forcing mechanism and sea ice influence need further investigation, perhaps best via a modeling framework.

To shed light on the nature of the upwelling on the Chukchi slope, we focus on the strongest event (event 9 in Table 3) which took place in May 2014. The composite averages for three stages of the event ('before', 'during', and 'after') are shown in Figs. 16–18. The 'before' composite is averaged over the 3 days preceding the upwelling event (Fig. 16). Prior to the event the wind was from the southwest and the wind stress curl was positive over much of the Chukchi shelf (Fig. 16e and f). The slope current was well established and the shelfbreak jet was reversed to the west (Fig. 16c). The direction of flow at the array line was mainly northwestward, with a cross-stream component that varied from site to site, predominantly offshore relative to the year-long mean direction (Fig. 16b).

During the upwelling event, the density at the shelfbreak (CS2) increased markedly with a maximum change of about 0.7 kg m^{-3} (Fig. 17a). The density at the outer shelf displayed a similar increase with a lag of roughly two days. The slope current remained strong and the reversed flow of the shelfbreak jet intensified (Fig. 17c). The most notable difference is that the flow veered onshore at all of the mooring sites (Fig. 17b). The cross-stream section shows that the onshore flow was present throughout the upper 200 m of the water column, and especially strong at the shelfbreak. The wind changed little, veering slightly to the east, and the wind stress curl remained positive on the Chukchi shelf.

At the conclusion of the upwelling event, the density at the shelfbreak and outer-shelf decreased back to their low-passed values (Fig. 18a). The slope current weakened and the southeastward-flowing shelfbreak jet re-established itself along with enhanced southeastward flow of Atlantic water at depth (Fig. 18c). The depth-integrated cross-stream flow was weak (Fig. 18b), but the structure of the flow was baroclinic, with offshore flow in the upper layer and onshore flow near the bottom (Fig. 18d). The wind in the vicinity of the array weakened and became more westerly, causing the wind stress curl on the Chukchi shelf to become negative (Fig. 18e and f).

The reader will notice that the conditions both leading up to the upwelling event and during the event are reminiscent of the

Table 3
Statistics of the upwelling events measured by the mooring array. The rows indicate: event number; length (in days) of each event; value of the upwelling index (UI, unit: kg m^{-3}h); and mean wind speed, direction, and sign of the mean wind stress curl in the vicinity of mooring array (magenta box in Fig. 2a) for the period from 3 days prior to each event to the end of the event (+and – denote positive (cyclonic) and negative (anti-cyclonic) curl, respectively).

Event	1	2	3	4	5	6	7	8	9	10	11	12	13	14	15	Mean
Length (d)	1.7	2.5	1.9	6	2.2	6.2	3.3	2	4.5	2.4	1.3	3.6	4.5	5.1	4.6	3.5
UI (kg m^{-3}h)	3.8	1.8	5.5	11.1	1.1	9.0	6.4	2.4	26.7	2.0	3.5	10.7	1.5	2.4	3.4	5.9
Wind speed (m s^{-1})	4.5	4.5	4.5	3.9	2.7	4.9	3.9	2.8	3.8	3.0	3.0	4.4	6.7	5.2	6.2	4.3
Wind direction	NE	SW	SW	NE	NW	NE	NE	SW	SW	NE	NE	SW	NE	SW	SW	SE
Wind stress curl	–	–	+	+	–	+	–	–	+	+	+	+	–	–	+	–

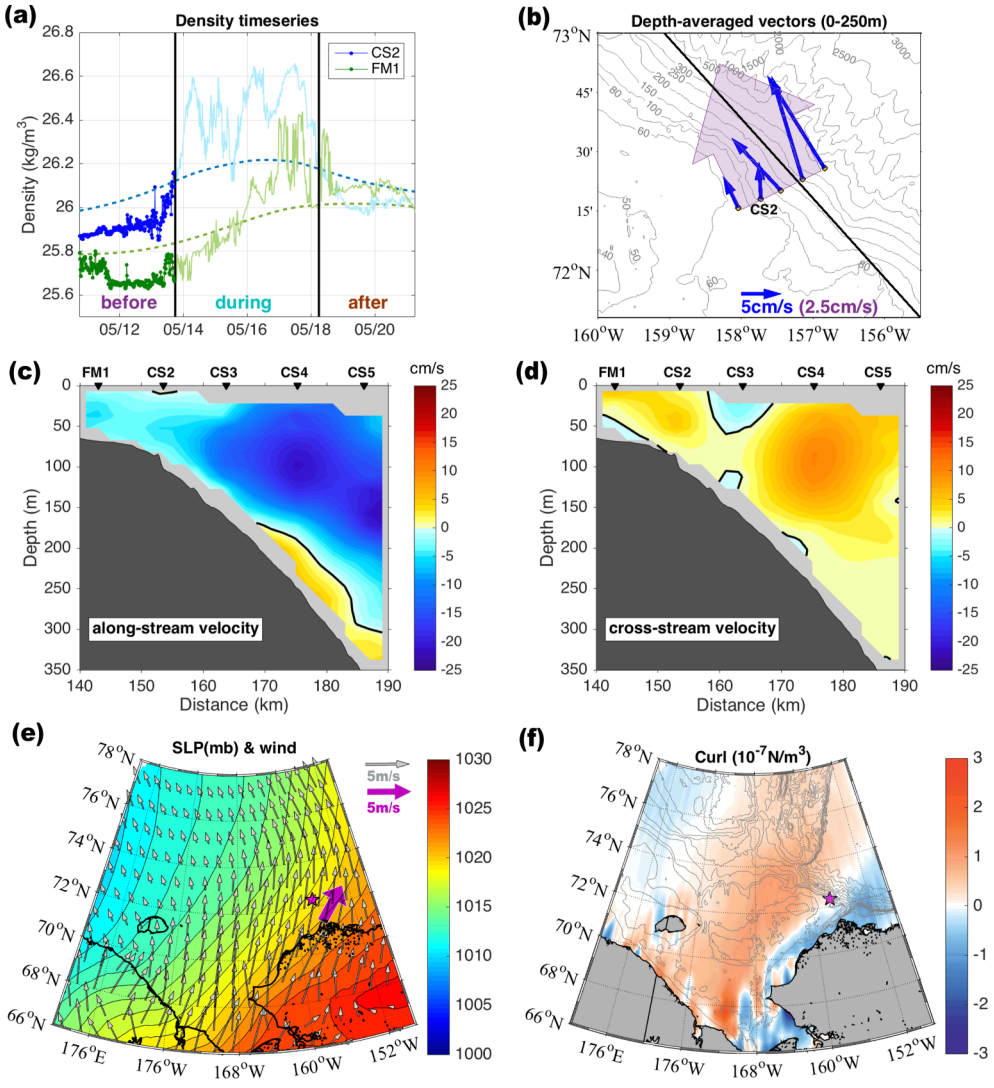

Fig. 16. Composite average fields prior to an upwelling event in May 2014 (event 9, see Table 3). (a) Density timeseries at the shelfbreak mooring CS2 and outer-shelf mooring FM1 from 3 days before the event to 3 days after the event, where the bold indicates the time period before the upwelling. The dashed lines are the 20-day low-passed curves. (b) Depth-averaged (0–250 m) velocity vectors at the mooring sites (blue arrows) and the mean velocity vector of all moorings (large arrow). The year-long mean velocity direction is denoted by the black line. (c) Vertical section of alongstream velocity. (d) Vertical section of cross-stream velocity (positive is offshore). (e) Sea level pressure (color) and 10 m-wind vectors from NARR (grey vectors), along with the measured wind from the Barrow meteorological station (purple vector). The location of the shelfbreak/slope mooring array is indicated by the purple star. (f) Wind stress curl (color). (For interpretation of the references to colour in this figure legend, the reader is referred to the web version of this article.)

southwesterly type of extreme event analyzed earlier (Fig. 10). In particular: a strengthened slope current, reversed shelfbreak jet, and positive wind stress curl on the Chukchi shelf. In fact, upwelling event 9 corresponded to an extreme event, prompting us to ask if all of the upwelling events were associated with extreme events. The answer is no. Most of the upwelling events occurred between extreme events, while there was some overlap with both kinds of extreme events. With regard to upwelling event 9, it is unclear what caused the flow to veer onshore during this event.

7. Propagation of water mass signals

As discussed in the introduction, while there is increasing evidence that the slope current is an important component of the regional circulation and that it appears to stem largely from the outflow from Barrow Canyon, its origin still needs to be confirmed observationally. While this is beyond the scope of the present study, we can address the timing of water mass signals between a mooring situated at the head of Barrow Canyon and our array on the Chukchi shelfbreak/slope. The Barrow Canyon mooring (mooring BC2 in Fig. 2) was positioned in the region of strongest flow entering the canyon (Weingartner et al., 2017). The year-long mean velocity was directed to the northeast (down-canyon, Fig. 3).

Using the temperature-salinity definitions in Fig. 4b, we compared the timeseries of water masses measured throughout the year at the head of Barrow Canyon (mooring BC2, 49 m), and in the Chukchi Slope Current (mooring CS4, depth range 50–235 m, Fig. 19). The most common water mass passing through the head of Barrow Canyon was newly-ventilated winter water (WW, keeping in mind that the MicroCAT was located near the bottom). This cold water mass was present almost exclusively in the canyon from the beginning of February to early-July (marked by the black triangles in Fig. 19a). Comparing this to the site of the Chukchi mooring array, one sees that the bulk of the WW appeared in the slope current from early-April to early-September (marked by the black triangles in Fig. 19b). Hence, the winter water was present at both locations for roughly five months, with an offset on the order of two months. This supports the notion advanced by Corlett and Pickart (2017), Watanabe et al. (2017), and Spall et al. (2018) that the outflow from Barrow Canyon feeds the slope current.

To investigate this further, we examined the variation in potential temperature of the WW at the two locations (Fig. 20). The first thing to note is that the water is systematically warmer on the Chukchi slope than in Barrow Canyon, by approximately 0.07 °C. This makes sense in that lateral mixing would warm the water as it exits Barrow Canyon and flows westward in the slope current. Furthermore, at both sites there is a clear moderation of the WW to warmer temperatures as the season progresses. We vertically averaged the moored profiler record at CS4 and compared this to the record at BC2. The strongest correlation between the two timeseries ($r = 0.6$, significant at the 95% confidence level) was found for a lag of 60 days (BC2 leading CS4). This is

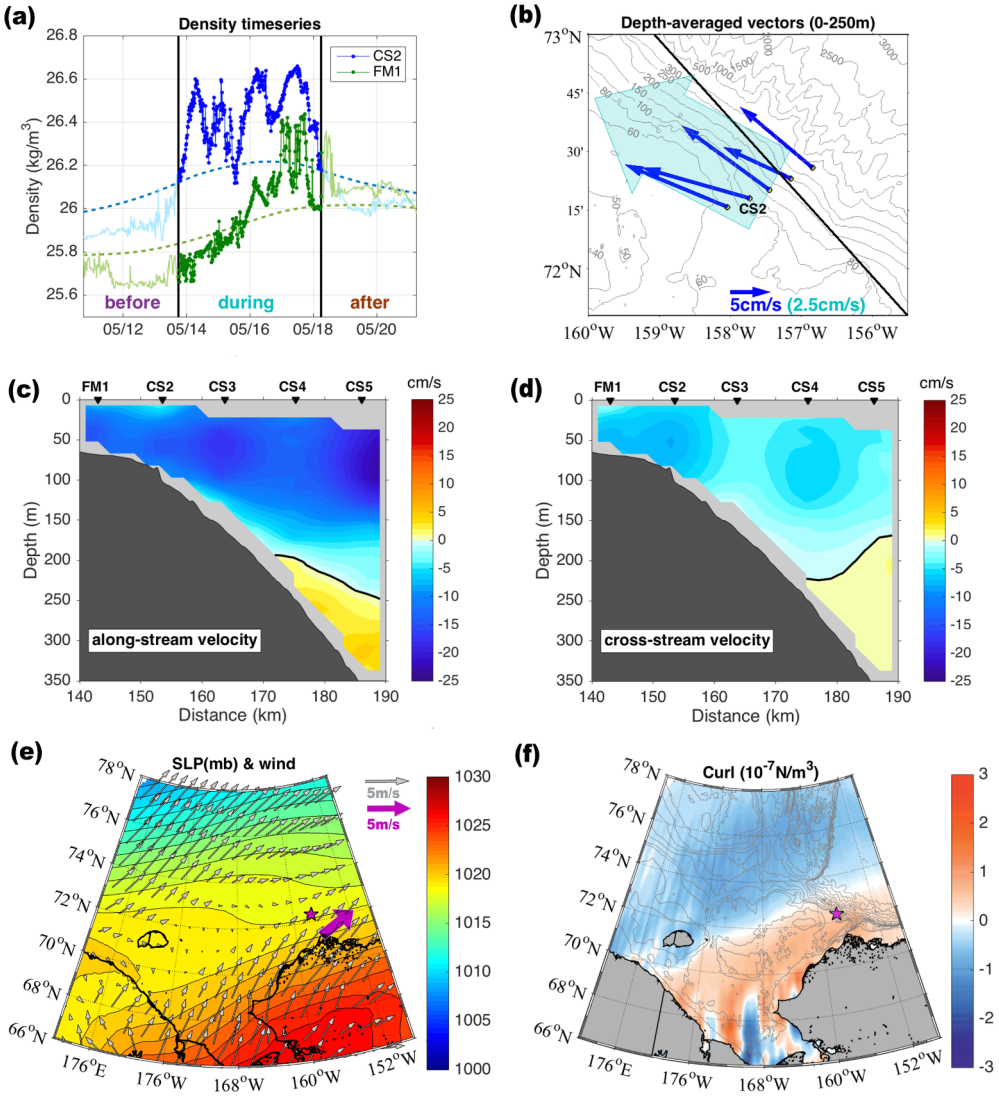

Fig. 17. Same as Fig. 16, except for the time period during the upwelling.

consistent with the offset noted above in the arrival times of the WW at the two sites.

The geographical distance from the head of Barrow Canyon to its mouth, plus the distance to the Chukchi slope array, is approximately 300 km. For a time lag of 60 days, this implies a mean advective speed of 5.6 cm/s. The mean velocity at BC2 during the WW period was 17.9 cm/s, which is considerably larger than this. However, it is probably more appropriate to use the velocity at the array site for this comparison. This is because the flow at head of the Barrow Canyon is locally convergent and the velocity there is stronger than farther down the canyon (Pickart et al., 2005). The velocity at CS4 averaged over the depth of the WW layer for the appropriate period is 9.3 cm/s, which is reasonably close to the above estimate deduced from the water mass signals.

8. Summary and discussion

Using timeseries from a set of moorings maintained from fall 2013 to fall 2014, the circulation and water mass properties in the vicinity of the Chukchi shelfbreak and slope were investigated. The Chukchi Shelfbreak Jet and the newly-identified Chukchi Slope Current were found to be year-round features with significant seasonal variation. The slope current is surface-intensified in summer and fall and middepth-intensified in winter and spring, during which time it moves shoreward and weakens. The year-long mean volume transport of the current was estimated to be 0.71 ± 0.05 Sv westward, with a Pacific water transport of 0.57 ± 0.04 Sv. The shelfbreak jet is a bottom-intensified current flowing to the east, with a mean transport of 0.009 ± 0.003 Sv. The transport weakens in the spring and becomes westward in May and June. The integrated flow from top to bottom in the vicinity of the shelfbreak is westward in the mean, with an average transport of 0.025 ± 0.008 Sv. The transport timeseries of the shelfbreak jet and slope current were found to be negatively correlated at a significant confidence level.

We identified two extreme states of the circulation which were reflected in the dominant EOF mode of alongstream velocity variability. The first state corresponds to an enhanced slope current and reversed (westward-flowing) shelfbreak jet, and the second state corresponds to a strong eastward-flowing shelfbreak jet and weak slope current. The former state occurs under both southwesterly and northeasterly winds, though in each case there is positive wind stress curl over the northeastern Chukchi shelf. The latter scenario occurs primarily under northeasterly winds when the wind stress curl over the shelf is negative. Using a simple theoretical model of the flow in the surface and bottom Ekman layers, we demonstrated that the changes in sea surface height on the shelf due to such wind stress curl forcing was consistent with the observed changes in flow seaward of the shelf – both in amplitude and phase – via geostrophic set up.

Applying a metric used in previous studies for identifying shelfbreak upwelling in the Beaufort Sea, we determined that there were 15

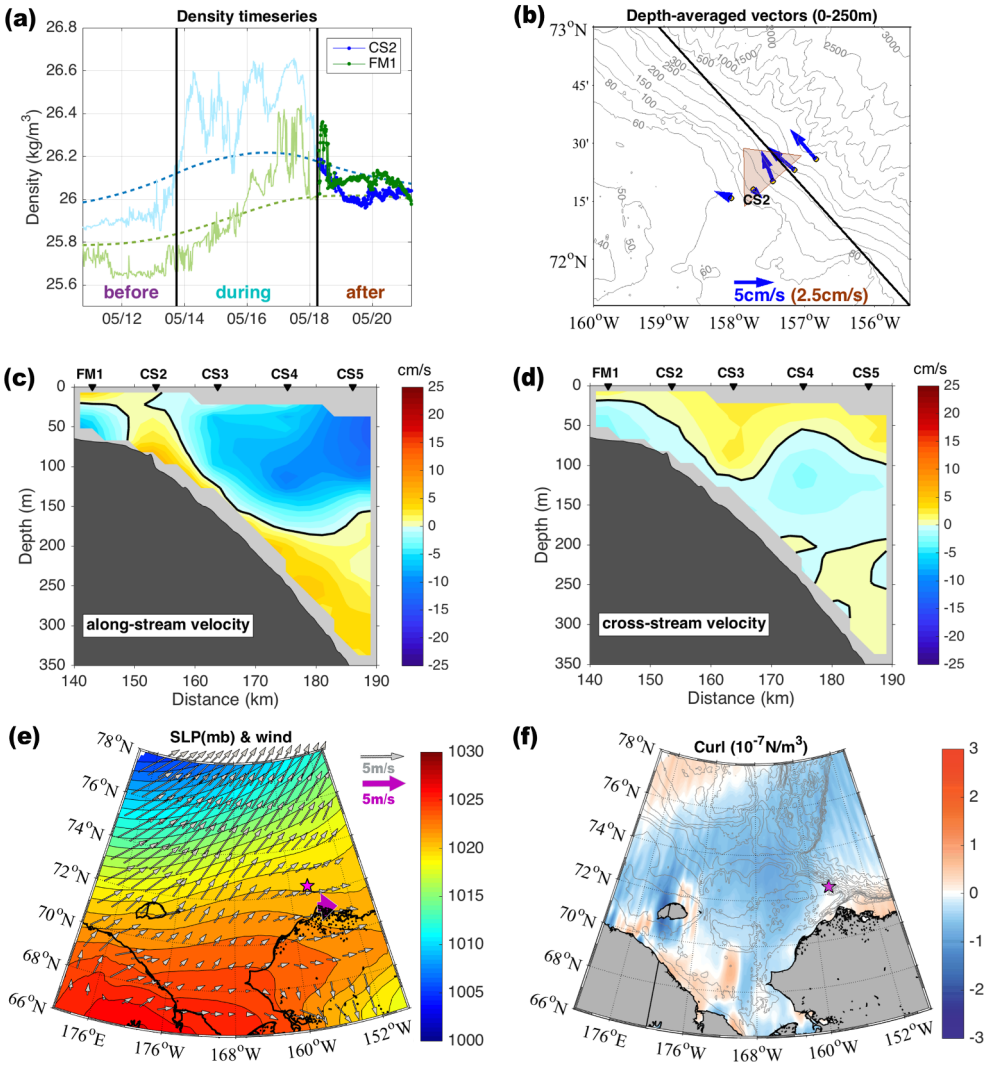

Fig. 18. Same as Fig. 16, except for the time period after the upwelling.

upwelling events over the course of the year at our array site at the edge of the Chukchi Sea. In contrast to the Beaufort Sea, there was no correlation between wind conditions and the upwelling. Furthermore, there was no apparent relationship between upwelling and the extreme slope current / shelfbreak jet events. While the strongest upwelling event did coincide with an extreme event (strong slope current, reversed shelfbreak jet), this was an exception not the rule, and it was unclear why the flow in this case veered strongly onshore. Further work is required to identify the causes of upwelling at the Chukchi shelfbreak.

The dominant water masses present at the shelfbreak/slope mooring site over the course of the year were newly-ventilated Pacific winter water, remnant winter water, and Atlantic water. The newly-ventilated

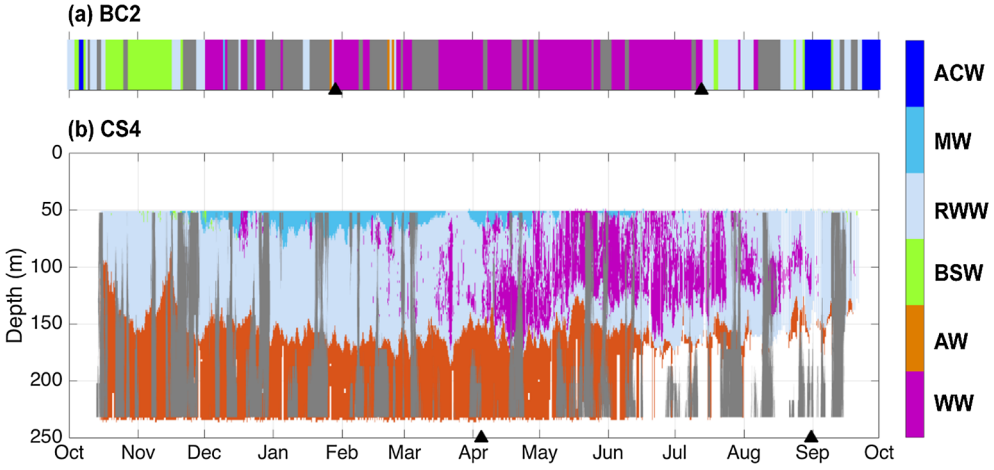

Fig. 19. Timeseries of water mass occurrence at (a) the head of Barrow Canyon (mooring BC2), and (b) in the Chukchi Slope Current (mooring CS4). See Figs. 2 and 3 for mooring locations. Note that there is no depth scale for BC2 since this site has a single sensor near the bottom (49 m). The gray shading indicates times when the flow is in the opposite direction of the predominant current (southwestward and southeastward in the two panels, respectively). The black triangles denote the time periods when the bulk of newly-ventilated winter water was present.

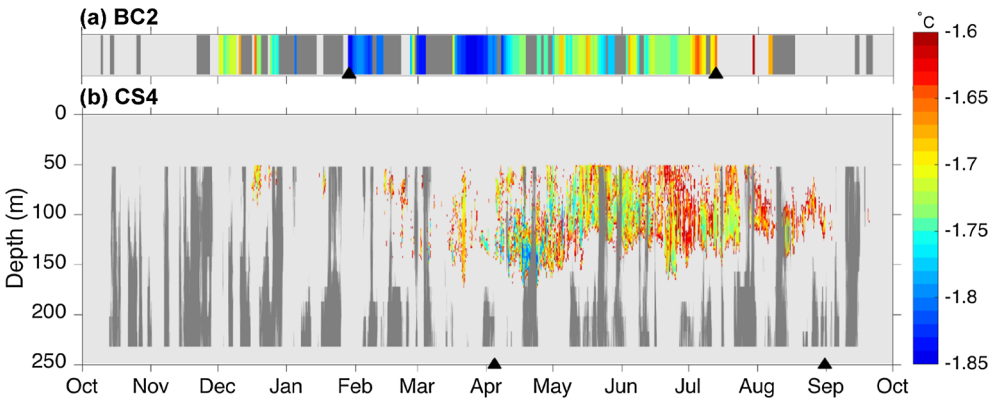

Fig. 20. Potential temperature of the newly-ventilated winter water at (a) mooring BC2 at head of Barrow Canyon (49 m, near the bottom) and (b) mooring CS4 on the Chukchi slope. The light gray shading means that there is no winter water present. The dark gray shading indicates when the flow is in the opposite direction of the primary current (southwestward and southeastward in (a) and (b), respectively). The black triangles denote the time periods when the bulk of winter water appeared.

winter water appeared in the slope current over the five-month period from early-April to early-September. This same water mass flowed northward through Barrow Canyon over the five-month period from early-February to early-July. Such a 60-day lag implies an advective speed that is reasonably close to the mean velocity of the slope current. This supports recent modeling results and surface drifter data suggesting that the slope current originates from the outflow of Pacific water from Barrow Canyon (Watanabe et al., 2017; Spall et al., 2018; Stabeno et al., 2018).

It remains to be determined why the location of the Chukchi Slope Current changes seasonally from being offshore and surface-intensified in summer/fall to onshore and middepth-intensified in winter/spring. The analysis of Corlett and Pickart (2017) suggested that the current is a meandering free jet during the summer months that is baroclinically unstable, but they could not address the seasonal stability characteristics of the flow. The vertical shift of current maximum may be related to the seasonal variation of the outflow from Barrow Canyon. Using mooring data from 2006 to 2007, Itoh et al. (2013) documented that the maximum depth of the current at the mouth of Barrow Canyon was near the surface in summer and early-fall, and deepened to the middle of the water column from November to mid-June. Furthermore, the Beaufort shelfbreak jet, which is fed from the outflow from Barrow Canyon, displays similar seasonal variation in the depth of the current maximum (Nikolopoulos et al., 2009). Nonetheless, further investigation is needed to help determine the connection between the outflow from Barrow Canyon and the Chukchi Slope Current.

Acknowledgements

The authors wish to thank the crews of the USCGC *Healy* and the *Norseman II* for the deployment and recovery of the Chukchi slope mooring array. Jacob Cass and Peter Winsor were especially helpful in these efforts. Frank Bahr and Daniel Torres processed the mooring data. Funding for the fieldwork and analysis was provided by the Bureau of Ocean and Energy Management under contract M12AC00008 (ML, RP, TW), by the National Science Foundation under grants ARC-0856244 and PLR-1504333 (RP, PL), and OCE-1533170 and PLR-1415489 (MAS); ML also received support from the National Natural Science Foundation of China (Grants 41506018, 41876005, 41676008), the National Key Research and Development Program of China under contract No. 2016YFC14011403, and the GASI Project under contract No. GASI-IPOVAI-04; GWKM was supported by the Natural Sciences and Engineering Research Council of Canada.

References

Aagaard, K., Carmack, E., 1989. The role of sea ice and other fresh water in the arctic circulation. J. Geophys. Res 94, 14485–14498. https://doi.org/10.1029/JC094iC10p14485.

Arrigo, K.R., Perovich, D.K., Pickart, R.S., Brown, Z., van Dijken, G., Lowry, K., Mills, M., Palmer, M., Balch, W., Bates, N., Benitez-Nelson, C., Brownlee, E., Frey, K., Laney, S., Mathis, J., Matsuoka, A., Mitchell, B., Moore, G.W.K., Reynolds, R., Sosik, H., Swift, J., 2014. Phytoplankton blooms beneath the sea ice in the Chukchi sea. Deep-Sea Res. II: Topical Stud. Oceanogr 105, 1–16.

Brugler, E.T., Pickart, R.S., Moore, G.W.K., Roberts, S., Weingartner, T.J., Statscewich, H., 2014. Seasonal to interannual variability of the pacific water boundary current in the Beaufort Sea. Prog. Oceanogr 127, 1–20.

Coachman, L., Aagaard, K., Tripp, R., 1975. Bering Strait: The Regional Physical Oceanography. University of Washington Press.

Corlett, W.B., Pickart, R.S., 2017. The Chukchi slope current. Prog. Oceanogr. 153, 50–56.

Fischer, J., Karstensen, J., Zantopp, R.J., Visbeck, M., Biastoch, A., Behrens, E., Böning, C.W., Quadfasel, D., Jochumsen, K., Valdimarsson, H., Jónsson, S., Bacon, S., Holliday, N.P., Dye, S., Rhein, M., Mertens, C., 2015. Intra-seasonal variability of the DWBC in the western subpolar North Atlantic. Prog. Oceanogr. 132, 233–249.

Ghil, M., Allen, R., Dettinger, M.D., Ide, K., Kondrashov, D., Mann, M.E., Robertson, A.W., Saunders, A., Tian, Y., Varadi, F., Yiou, P., 2002. Advanced spectral methods for climatic timeseries. Rev. Geophys. 40 (1), 1003. https://doi.org/10.1029/2000RG000092.

Gong, D., Pickart, R.S., 2015. Summertime circulation in the eastern Chukchi Sea. Deep-Sea Res. II 118, 18–31.

Gong, D., Pickart, R.S., 2016. Early summer water mass transformation in the eastern Chukchi Sea. Deep-Sea Res. II 130, 43–55.

Harden, B.E., Pickart, R.S., 2018. High-frequency variability in the North Icelandic jet. J. Mar. Res. 76, 47–62.

Hassani, H., 2007. Singular spectrum analysis: methodology and comparison. J. Data Sci. 5, 239–257.

Hill, V.J., Cota, G.F., 2005. Spatial patterns of primary production on the shelf, slope and basin of the western Arctic in 2002. Deep-Sea Res. II 52, 3344–3354.

Isachsen, P.E., LaCasce, J.H., Mauritzen, C., Häkkinen, S., 2003. Wind-driven variability of hte large-scale recirculating flow in the Nordic Seas and Arctic Ocean. J. Phys. Oceanogr. 33, 2534–2550.

Itoh, M., Shimada, K., Kamoshida, T., McLaughlin, F., Carmack, E., Nishino, S., 2012. Interannual variability of Pacific winter water inflow through Barrow Canyon from 2000 to 2006. J. Oceanogr. 68, 575–592.

Itoh, M., Nishino, S., Kawaguchi, Y., Kikuchi, T., 2013. Barrow Canyon volume, heat, and freshwater fluxes revealed by long-term mooring observations between 2000 and 2008. J. Geophys. Res. 118, 4363–4379. https://doi.org/10.1002/jgrc.20290.

Johns, W.E., Watts, D.R., 1986. Time Scales and structure of topographic Rossby waves and meanders in the deep Gulf Stream. J. Mar. Res. 44, 267–290.

Jones, E.P., Anderson, L.G., 1986. On the origin of the chemical properties of the Arctic Ocean halocline. J. Geophys. Res. 91 10,759–10,767.

Lin, P., Pickart, R., Moore, K., Spall, M., Hu, J., 2018. Characteristics and Dynamics of wind-driven upwelling in the Alaskan Beaufort Sea based on six years of mooring data. Deep-Sea Res. II. https://doi.org/10.1016/j.dsr2.2018.01.002.

Linders, J., Pickart, R.S., Björk, G., Moore, G.W.K., 2017. On the nature and origin of water masses in Herald Canyon, Chukchi Sea: synoptic surveys in summer 2004, 2008, and 2009. Prog. Oceanogr. 159, 99–114.

Llinás, L., Pickart, R.S., Mathis, J.T., Smith, S.L., 2009. Zooplankton inside an arctic cold-core eddy: probable origin and fate. Deep-Sea Res. II 56, 1290–1304.

Marshall, J.C., Hill, C., Perelman, L., Adcroft, A., 1997. Hydrostatic, quasi-hydrostatic, and non-hydrostatic ocean modeling. J. Geophys. Res. 102, 5733–5752.

Mathis, J.T., Pickart, R.S., Hansell, D.A., Kadko, D., Bates, N.R., 2007. Eddy transport of organic carbon and nutrients from the Chukchi shelf into the deep Arctic basin. J. Geophys. Res. 112. https://doi.org/10.1029/2006JC00,389.

Mesinger, F., DiMego, G., Kalnay, E., Mitchell, K., Shafran, P.C., Ebisuzaki, W., Jović, D., Woollen, J., Rogers, E., Berbery, E.H., Ek, M.B., Fan, Y., Grumbine, R., Higgins, W., Li, H., Lin, Y., Manikin, G., Parrish, D., Shi, W., 2006. North American regional re-analysis. Bull. Amer. Meteor. Soc. 87, 343–360.

Muench, R.D., Schumacher, J.D., Salo, S.A., 1988. Winter currents and hydrographic conditions on the northern central bering sea shelf. J. Geophys. Res. Oceans 93, 516–526.

Nikolopoulos, A., Pickart, R.S., Fratantoni, P.S., Shimada, K., Torres, D.J., Jones, E.P., 2009. The western arctic boundary current at 152°w: structure, variability, and transport. Deep-Sea Res. II 56, 1164–1181.

Nöst, O.A., Isachsen, P.E., 2003. The large-scale time-mean ocean circulation in the Nordic Seas and Arctic Ocean estiamted from simplified dynamics. J. Mar. Res. 61,

175–210.
Pacini, A., Pickart, R.S., Moore, G.W.K., Våge, K., 2016. Hydrographic structure and modification of Pacific winter water on the Chukchi Sea shelf in late spring. Eos Trans. AGU abstract, H14B–1406.
Paquette, R.G., Bourke, R.H., 1974. Observations on the coastal current of Arctic Alaska. J. Mar. Res. 32, 195–207.
Pawlowicz, R., Beardsley, B., Lentz, S., 2002. Classical tidal harmonic analysis including error estimates in MATLAB using T_TIDE. Comput. Geosci. 28, 929–937.
Pickart, R.S., 2004. Shelfbreak circulation in the Alaskan Beaufort Sea: mean structure and variability. J. Geophys. Res 109, C04024. https://doi.org/10.1029/2003JC001912.
Pickart, R.S., Weingartner, T., Pratt, L., Zimmermann, S., Torres, D., 2005. Flow of winter-transformed pacific water into the western arctic. Deep-Sea Res. II 52, 3175–3198.
Pickart, R., Moore, G., Torres, D., Fratantoni, P., Goldsmith, R., Yang, J., 2009. Upwelling on the continental slope of the Alaskan Beaufort Sea: storms, ice, and oceanographic response. J. Geophys. Res. 114, C00A13. https://doi.org/10.1029/2008JC005 009.
Pickart, R.S., Pratt, L.J., Torres, D.J., Whitledge, T.E., Proshutinsky, A.Y., Aagaard, K., Agnew, T.A., Moore, G.W.K., Dail, H.J., 2010. Evolution and dynamics of the flow through Herald Canyon in the western Chukchi sea. Deep-Sea Res. II 57, 5–26.
Pickart, R., Spall, M., Moore, G., Weingartner, T., Woodgate, R., Aagaard, K., Shimada, K., 2011. Upwelling in the Alaskan Beaufort Sea: atmospheric forcing and local versus non-local response. Prog. Oceanogr. 88, 78–100.
Pickart, R.S., Schulze, L.M., Moore, G.W.K., Charette, M.A., Arrigo, K.R., van Dijken, G., Danielson, S.L., 2013. Long-term trends of upwelling and impacts on primary productivity in the Alaskan Beaufort Sea. Deep-Sea Res. I 79, 106–121.
Pickart, R.S., Moore, G.W.K., Mao, C., Bahr, F., Nobre, C., Weingartner, T.J., 2016. Circulation of winter water on the Chukchi shelf in early summer. Deep-Sea Res. II 130, 56–75.
Pisareva, M.N., Pickart, R.S., Spall, M., Nobre, C., Torres, D., Moore, G.W.K., Whitledge, T.E., 2015. Flow of pacific water in the western chukchi sea: results from the 2009 rusalca expedition. Deep-Sea Res. I 105, 53–73.
Schulze, L.M., Pickart, R.S., 2012. Seasonal variation of upwelling in the Alaskan Beaufort Sea: impact of sea ice cover. J. Geophys. Res. 117. https://doi.org/10.1029/2012JC007 985.
Shimada, K., Kamoshida, T., Itoh, M., Nishino, S., Carmack, E., McLaughlin, F., Zimmermann, S., Proshutinsky, A., 2006. Pacific Ocean inflow: influence on catastrophic reduction of sea ice cover in the Arctic Ocean. Geophys. Res. Lett. 33, L08605. https://doi.org/10.1029/2005GL025 624.
Spall, M.A., 2007. Circulation and water mass transformation in a model of the Chukchi Sea. J. Geophys. Res. 112, C05025. https://doi.org/10.1029/2005JC003364.
Spall, M.A., Pickart, R.S., Fratantoni, P.S., Plueddemann, A.J., 2008. Western Arctic shelfbreak eddies: formation and transport. J. Phys. Oceanogr. 38, 1644–1668.
Spall, M.A., Pickart, R.S., Brugler, E.T., Moore, G.W.K., Thomas, L., Arrigo, K.R., 2014. Role of shelfbreak upwelling in the formation of a massive under-ice bloom in the Chukchi Sea. Deep-Sea Res. II 105, 17–29.
Spall, M.A., 2016. Wind-driven flow over topography. J. Mar. Res. 74, 229–248.
Spall, M.A., Pickart, R.S., Li, M., Itoh, M., Lin, P., Kikuchi, T., Qi, Y., 2018. Transport of Pacific water into the Canada Basin and the formation of the Chukchi Slope Current. J. Geophys. Res. 123, 7453–7471.
Stabeno, P., Kachel, N., Ladd, C., Woodgate, R., 2018. Flow patterns in the eastern Chukchi Sea: 2010–2015. J. Geophys. Res. 123, 1177–1195.
Steele, M., Morison, J., Ermold, W., Rigor, I., Ortmeyer, M., Shimada, K., 2004. Circulation of summer pacific halocline water in the Arctic Ocean. J. Geophys. Res. 109, C02027. https://doi.org/10.1029/2003JC002009.
Stigebrandt, A., 1984. The north pacific: a global-scale estuary. J. Phys. Oceanogr. 14, 464–470.
Timmermans, M.-L., Proshutinsky, A., Golubeva, E., Jackson, J.M., Krishfield, R., McCall, M., Platov, G., Toole, J., Williams, W., Kikuchi, T., Nishino, S., 2014. Mechanisms of Pacific summer water variability in the Arctic's central Canada basin. J. Geophys. Res. 119, 7523–7548.
Timmermans, M.-L., Marshall, J., Proshutinsky, A., Scott, J., 2017. Seasonally derived components of the Canada Basin halocline. Geophys. Res. Lett. 44, 5008–5015. https://doi.org/10.1002/2017GL073042.
Toole, J., Timmermans, M.-L., Perovich, D., Krishfield, R., Proshutinsky, A., Richter-Menge, J., 2010. Influences of the ocean surface mixed layer and thermohaline stratification on Arctic sea ice in the central Canada Basin. J. Geophys. Res. 115, C10018. https://doi.org/10.1029/2009JC005660.
Tschudi, M., Fowler, C., Maslanik, J., Stewart, J.S., Meier, W., Polar Pathfinder Daily 25 km EASE-Grid Sea Ice Motion Vectors, Version 3, 2016. Boulder, Colorado USA. NASA National Snow and Ice Data Center Distributed Active Archive Center. https://doi.org/10.5067/O57VAIT2AYYY.
Walsh, J.J., 1995. DOC storage in Arctic seas: the role of continental shelves. In: Smith, W.O., Grebmeier, J.M. (Eds.), Arctic Oceanography: Marginal Ice Zones and Continental Shelves. American Geophysical Union, Washington, DC, pp. 203–230.
Watanabe, E., Onodera, J., Itoh, M., Nishino, S., Kikuchi, T., 2017. Winter transport of subsurface warm water toward the Arctic Chukchi Borderland. Deep-Sea Res. I 128, 115–130.
Weingartner, T.J., Cavalieri, D.J., Aagaard, K., Sasaki, Y., 1998. Circulation, dense water formation, and outflow on the northeast Chukchi shelf. J. Geophys. Res. 103, 7647–7661.
Weingartner, T.J., Aagaard, K., Woodgate, R.A., Danielson, S., Sasaki, Y., Cavalieri, D., 2005. Circulation on the north central Chukchi sea shelf. Deep-Sea Res. II 52, 3150–3174.
Weingartner, T., Dobbins, E., Danielson, S., Winsor, P., Potter, R., Statscewich, H., 2013. Hydrographic variability over the northeastern Chukchi Sea shelf in summer-fall 2008–2010. Cont. Shelf Res. 67, 5–22.
Weingartner, T.J., Potter, R.A., Stoudt, C.A., Dobbins, E.L., Statscewich, H., Winsor, P.R., Mudge, T.D., Borg, K., 2017. Transport and thermohaline variability in Barrow Canyon on the Northeastern Chukchi Sea Shelf. J. Geophys. Res. 122, 3565–3585. https://doi.org/10.1002/2016JC012636.
Woodgate, R.A., Aagaard, K., Weingartner, T.J., 2005. A year in the physical oceanography of the Chukchi Sea: moored measurements from autumn 1990–1991. Deep-Sea Res. II 52, 3116–3149.
Woodgate, R.A., Weingartner, T., Lindsay, R., 2010. The 2007 Bering Strait oceanic heat flux and anomalous Arctic sea-ice retreat. Geophys. Res. Lett. 37, L01602. https://doi.org/10.1029/2009GL041 621.
Yang, J., 2006. The seasonal variability of the Arctic Ocean Ekman transport and its role in the mixed layer heat and salt fluxes. J. Climate 19, 5366–5387.